Robust Hamiltonian Engineering for Interacting Qudit Systems

Hengyun Zhou,[1,*] Haoyang Gao,[1,*] Nathaniel T. Leitao,[1] Oksana Makarova,[1,2] Iris Cong,[1] Alexander M. Douglas,[1] Leigh S. Martin,[1] and Mikhail D. Lukin[1]

[1]*Department of Physics, Harvard University, Cambridge, Massachusetts 02138, USA*
[2]*School of Engineering and Applied Sciences, Harvard University, Cambridge, Massachusetts 02138, USA*

(Received 30 September 2023; revised 11 April 2024; accepted 30 May 2024; published 31 July 2024)

Dynamical decoupling and Hamiltonian engineering are well-established techniques that have been used to control qubit systems. However, designing the corresponding methods for qudit systems has been challenging due to the lack of a Bloch sphere representation, more complex interactions, and additional control constraints. By identifying several general structures associated with such problems, we develop a formalism for the robust dynamical decoupling and Hamiltonian engineering of strongly interacting qudit systems. Our formalism significantly simplifies qudit pulse-sequence design while naturally incorporating robustness conditions necessary for experimental practicality. We experimentally demonstrate these techniques in a strongly interacting, disordered ensemble of spin-1 nitrogen-vacancy centers, achieving more than an order-of-magnitude improvement in coherence time over existing pulse sequences. We further describe how our techniques enable the engineering of exotic many-body phenomena such as quantum many-body scars, and open up new opportunities for quantum metrology with enhanced sensitivities. These results enable wide-reaching new applications for dynamical decoupling and Hamiltonian engineering in many-body physics and quantum metrology.

DOI: 10.1103/PhysRevX.14.031017

Subject Areas: Atomic and Molecular Physics, Quantum Physics, Quantum Information

I. INTRODUCTION

The design and implementation of novel Hamiltonians opens up a wide range of opportunities in quantum science and engineering. Examples range from twisting Hamiltonians for entanglement-enhanced quantum metrology [1–3] and the toric code Hamiltonian for quantum computation [4–6] to various XXZ spin-chain models for quantum many-body physics [7–9]. One approach to the experimental implementation of such models is to build specific quantum simulator systems, where the desired Hamiltonian is directly realized in the system [10–12]. An alternative approach is to start with the native Hamiltonian of a system and employ so-called Hamiltonian engineering techniques to transform this native Hamiltonian into a desired form [13,14]. Such methods are examples of Floquet engineering and have emerged as a powerful way to turn a quantum simulator of one specific Hamiltonian into a simulator of many desired systems [15–19]. As a special case of Hamiltonian engineering, dynamical decoupling of interactions [20–24] plays a particularly important role, both in preserving the state of the system when needed and as a key step towards the engineering of more complex interaction Hamiltonians.

Until now, the majority of existing Hamiltonian engineering methods for spin systems have focused on qubits, due to their ease of manipulation, the availability of geometric intuition from the Bloch sphere, relevance to many experimental systems, as well as maturity of control techniques originally developed in the nuclear magnetic resonance (NMR) community [20,23–30]. Extending these techniques to qudit systems with more than two states presents several new opportunities [22]. For quantum many-body physics, qudits enable a richer landscape of Hamiltonians [31], allowing for new explorations of quantum many-body scars [32–34], quantum chaos [35], and additional spin-exchange channels [36,37]. In quantum metrology, the larger spin results in a larger dipole moment for enhanced sensitivity [38–40] and may also allow time-reversal operations required in certain protocols that are not readily accessible with two levels [22,41,42]. Moreover, such techniques will also be relevant for a large number of experimental platforms, including nitrogen-vacancy (NV) centers in diamond (spin-1) [38–40,43], quadrupolar NMR (^{2}H, ^{14}N have nuclear spin-1) [44–46], cold molecules [47,48], and nuclear spins or hyperfine states in trapped atoms and ions [49–53].

[*]These authors contributed equally to this work.

Designing qudit Hamiltonian engineering sequences, however, is significantly more challenging. Indeed, despite ample motivation in quadrupolar NMR (e.g., ^{14}N) and the use of qubit interaction decoupling sequences like WAHUHA [20] for over 50 years, its qutrit counterpart was only discovered recently [22,54]. Moreover, these qutrit sequences do not take into account any practical robustness considerations, making their implementation and application challenging in practice (see, e.g., Fig. 8). Consequently, while there has been work on single-qudit dynamical decoupling [44–46,55–58], up to now there have been no experimental demonstrations of full disorder and interaction decoupling for interacting spin systems with more than two levels.

One major obstacle to designing qudit Hamiltonian engineering sequences is the lack of a simple Bloch sphere picture, which makes the design procedure much less intuitive [59–64]. At the same time, the significantly larger Hilbert space leads to much more complicated Hamiltonians, involving flip-flops between any pair of states, whose analysis becomes qualitatively harder than the qubit case (see Sec. II). In addition, because of selection rule constraints, control is often available only on a subset of transitions, which limits the family of pulses we can use in sequence design. Moreover, even if it were possible to design sequences to engineer Hamiltonians in the case of ideal pulses, it is not clear whether they could be made robust to experimental imperfections such as finite pulse durations and other pulse errors.

To overcome these obstacles, we identify several key structures in the qudit Hamiltonian engineering problem and develop a general formalism for the task based on them. More specifically, motivated by recent advances in the robust Hamiltonian engineering of disordered and interacting qubit systems [17], we devise a representation of qudit Hamiltonian transformations based on the interaction picture transformations of the S^z operator, for any secular interaction Hamiltonian [i.e., Hamiltonians satisfying the rotating wave approximation (RWA)]. We find that the implementation of such transformations and the corresponding analysis of finite-pulse-duration effects and other imperfections can be easily achieved with a graphical representation of the desired transformations, where pulse sequences represent a walk through the graph that starts and ends at the same vertex [Figs. 3(b) and 3(e)]. The details of these structures and the formalism will be discussed in Sec. III.

Using this formalism, we design robust Hamiltonian engineering pulse sequences and, for the first time, experimentally demonstrate practical decoupling of spin-1 dipolar interactions. In particular, we successfully build a pulse sequence that not only decouples both on-site disorder and dipolar interactions but also achieves robustness against control errors and disorder during pulses. We experimentally implement this sequence in a disordered, interacting ensemble of spin-1 NV centers in diamond [Fig. 1(a)], a leading platform for quantum metrology [65], and quantum simulation of dipolar-interacting spin systems [43,66]. We compare the performance of our sequence [Fig. 1(c)] to existing sequences [22,66] and observe an order-of-magnitude improvement in the coherence time [Fig. 1(b)]. The significant improvement, in the presence of large disorder and control constrained by selection rules, highlights the power of our method.

The ability to robustly engineer qudit Hamiltonians represents an important step towards the realization of complex interaction Hamiltonians for quantum many-body physics and quantum metrology, and we describe how our techniques can be employed in these applications. As a demonstration of the rich landscape of Hamiltonians now accessible in qudit systems, we devise pulse sequences that transform the native NV-NV interaction between two groups of NVs with different lattice orientations into a spin-1 XY Hamiltonian, realizing an exotic, bipartite quantum many-body scar [32]. For quantum metrology, we discuss how higher spin systems naturally lead to an enhanced effective dipole moment for magnetic field sensing and how to maximize sensitivity given the complicated transformations of the Hamiltonian enacted by the pulse sequences [68].

This paper is organized as follows: In Sec. II, we compare the qudit case to the qubit case to motivate finding new structures to the qudit problem, in the absence of the Bloch sphere. In Sec. III, we introduce our general formalism for designing robust sequences in qudit systems, focusing on three key insights that enable robust sequence design. In Sec. IV, we analyze a specific example of qutrit decoupling sequence design, and in Sec. V, we demonstrate experimentally significant improvements in decoupling performance over existing pulse sequences. We then apply these techniques to quantum many-body physics and quantum metrology in Secs. VI and VII, and conclude in Sec. VIII with an outlook for future directions.

II. QUDIT VS QUBIT: IMPORTANCE OF STRUCTURE

The area of Hamiltonian engineering and dynamical decoupling has been developed for over half a century in the NMR community [20,23–30], leading to many pulse sequences with good performance and high robustness against control imperfections, including XY-8 [25], WAHUHA [20], MREV-8 [27], DROID [17], etc. However, this work has almost exclusively focused on the qubit case, despite the relevance of the more general qudit case to a variety of experimental systems, including, e.g., ^{14}N nuclear spins in NMR. The few exceptions [22,54] studying the qutrit case suffer from the use of complicated brute-force searches and limited performance in the presence of control imperfections. In this section, we will highlight four major reasons why the qudit case is

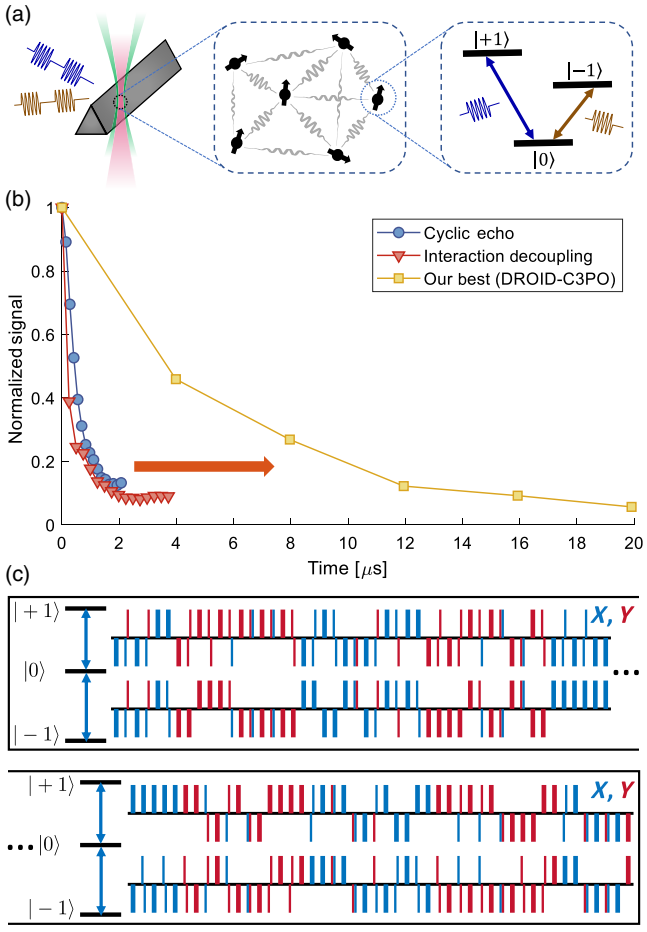

FIG. 1. Order-of-magnitude qutrit coherence improvement. (a) Experiment performed in an interacting NV-center ensemble in diamond. NV centers are spin-1 particles, and we use two microwave tones to drive the $|0\rangle \leftrightarrow |1\rangle$ and $|0\rangle \leftrightarrow |-1\rangle$ transitions, respectively. (b) Experimental demonstration of an order-of-magnitude improvement in decoupling timescale compared to existing sequences. The plotted curve is the measured average decay trace for different pulse sequences, where the average is taken over all three coherent superposition initial states $|0\rangle + |-1\rangle/\sqrt{2}$, $|0\rangle + |+1\rangle/\sqrt{2}$, and $|+1\rangle + |-1\rangle/\sqrt{2}$. (c) Plot of our current best qutrit decoupling sequence "DROID-C3PO" (i.e., disorder-robust interaction decoupling–coherent 3-level pulse optimization). All pulses in this pulse sequence simultaneously drive the two transitions with equal amplitude. The thin lines represent spin-$1\pi/2$ pulses (i.e., rotation of the spin-1 generalized Bloch sphere [22,67] by an angle $\pi/2$, experimentally implemented by simultaneously driving the two transitions with two $\pi/\sqrt{2}$ pulses), and the thick lines represent spin-1π pulses. The color of the pulses represents the pulse axis (X or Y), and the direction of the pulses (up or down) represents the two opposite rotation directions (e.g., $+\pi/2$ pulse and $-\pi/2$ pulse). The proportions of this plot are drawn consistently with actual time durations. The ellipsis in the plot indicates that the two rows are connected.

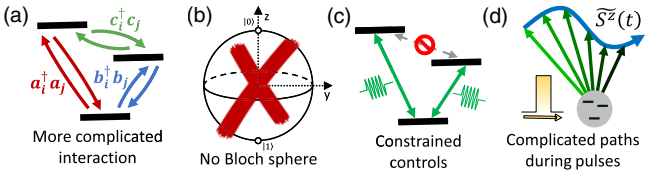

FIG. 2. Main challenges in the qudit case. (a) Qudit interactions involve flip-flop terms on every transition, together with multiple types of Ising-like terms, making the analysis of their transformation under pulses qualitatively harder. (b) The lack of a Bloch sphere picture makes the design procedure much less intuitive. (c) Available controls are constrained by the selection rules. (d) The complicated trajectories of the frame during pulses (the color gradient represents time during pulses) makes the incorporation of robustness conditions much harder.

qualitatively harder than the qubit case, as is also illustrated in Fig. 2.

A. More complex interactions

The more complex form of the interaction in the qudit case makes it qualitatively harder to analyze. To see this, let us first review the simpler qubit case, where the native Hamiltonian of the system can be written as

$$\hat{H}_0 = \sum_i h_i \hat{S}_i^z + \sum_{ij} J_{ij} \hat{S}_i^z \hat{S}_j^z . \tag{1}$$

The first term is an on-site disorder term, and the second term is an Ising interaction between the qubits. We emphasize that such a Hamiltonian form is the most generic symmetric secular qubit Hamiltonian (i.e., satisfying the RWA approximation), up to a Heisenberg part $\vec{S}_i \cdot \vec{S}_j$ that is invariant under pulses due to its SU(2) symmetry [22].

To perform Hamiltonian engineering, one typically goes into the interaction picture with respect to the pulses $\{\hat{P}_n\}$, where the Hamiltonian transforms as $\tilde{H}_k = U_{k-1}^\dagger H_0 U_{k-1}$, with $U_{k-1} = P_{k-1} \cdots P_1$ being the accumulated pulse unitaries. Examining the form of the native Hamiltonian, Eq. (1), it is obvious that the transformation of the full Hamiltonian is uniquely determined by the transformation of the S^z operator $\tilde{S}^z = U^\dagger S^z U$, which is referred to as the "frame" in the literature [17,69]. For example, $\tilde{S}^z = S^x$ leads to the Hamiltonian $\tilde{H} = \sum_i h_i \hat{S}_i^x + \sum_{ij} J_{ij} \hat{S}_i^x \hat{S}_j^x$. Engineering a target qubit Hamiltonian then simply consists of spending a specified amount of time in the X, Y, Z frames [17,20,70,71] to target a specific ratio between the Hamiltonian terms.

In the qudit case, however, the Hamiltonian becomes much more complicated. For example, the most generic secular qutrit Hamiltonian involves all three flip-flop terms

between $|0\rangle \leftrightarrow |1\rangle$, $|0\rangle \leftrightarrow |-1\rangle$, and $|-1\rangle \leftrightarrow |1\rangle$, whose transformation under unitaries becomes much more complicated than Eq. (1). Indeed, the explicit expression for the Hamiltonian transformation, which we tabulate in Appendix A 6, is over 4 pages long, compared to the one-liner in the qubit case. The complexity of these expressions suggests the importance of more systematically understanding the structure of qudit Hamiltonian engineering. Thus, unlike all existing works on qudit sequence design, which focus on unitaries instead of frames, we prove that the transformation of the Hamiltonian $\tilde{H}$ is still uniquely determined by the frame transformation $\tilde{S}^z$ (see Sec. III. 1 and Appendix A 3). This finding allows us to obtain a much more succinct description of the transformed Hamiltonian and significantly reduce the complexity of qudit Hamiltonian engineering.

B. Lack of Bloch sphere picture

For qubits, the choice of frames is straightforward based on the Bloch sphere picture: We simply choose the cardinal directions along X, Y, Z, which have a high degree of symmetry. To build a pulse sequence, one just needs to connect the X, Y, Z frames with pulses, where π pulses and $\pi/2$ pulses are the obvious choices based on the Bloch sphere geometry. In a sense, the Bloch sphere picture serves as a backbone, on which the design of pulse sequences is converted to the design of trajectories on the Bloch sphere.

In the qudit case, however, there is no longer an obvious candidate for the Bloch sphere: The naive generalization is an eight-dimensional object [22,67] that is not particularly informative. Although existing methods can find the necessary unitaries to engineer the target Hamiltonian, it is achieved by a brute-force search, as depicted in Fig. 3(d). Therefore, it does not organize those unitaries in any structured way similar to the Bloch sphere picture. In this method, one starts with a pulse set that may not be experimentally accessible (e.g., $\pi/2$ pulses on all transitions) and searches over the entire space of unitaries generated by them. Linear programming techniques are used to find a subset of unitaries that transform the native Hamiltonian to the desired form. As a result, the connection between these unitaries often involves complicated composite pulses that might go all the way back to the

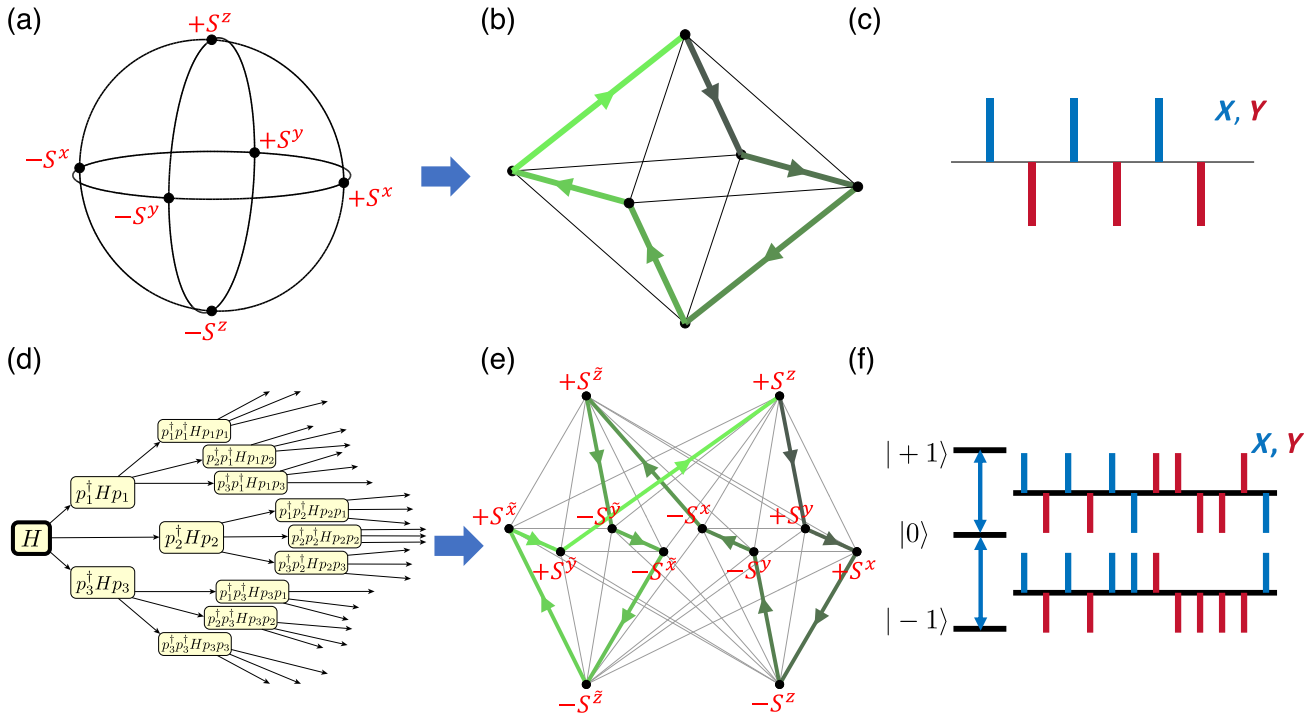

FIG. 3. Decoupling frame graphs. Geometric representation of decoupling pulse sequences. Vertices indicate transformed S^z frames, and edges indicate physically implementable pulses that connect different frames. (a)–(c) Representative qubit decoupling sequence. The Bloch sphere picture in diagram (a) naturally leads to the decoupling frame graph in diagram (b), by trivially replacing all arcs with a straight line. A walk on the decoupling frame graph (walk ordering given by color gradient and arrows) produces a pulse sequence consisting of $\pi/2$ pulses (c). (d)–(f) Corresponding results for a qutrit decoupling sequence. Because of the lack of a Bloch sphere picture, existing methods rely on the structureless brute-force search shown in diagram (d), which significantly limits the success of pulse-sequence design so far. The decoupling frame graph in diagram (e) captures the structures of the problem and serves as the backbone on which pulse sequences are designed [diagram (f)], in a way similar to the qubit case. These plots are only for high-level illustration of our methods; the details of qutrit decoupling sequence design are discussed in Sec. IV, and the precise definition of the frame set in diagram (e) is given in Eq. (10).

root node in Fig. 3(d), which requires cumbersome and structureless algebraic simplifications. Therefore, synthesizing the required unitaries has been a tricky and painful process, even without considering the actual performance of the sequence.

C. Constrained controls due to selection rules

Another unique limitation in the qudit case is the presence of selection rules, which constrain the available transitions we can drive. The consequence is that generic pairs of unitaries or frames cannot be directly connected via a single pulse, leading to the need of composite pulses or lambda-type drivings with a virtual intermediate level, both making the experiment much more complicated. As a specific example of pulse-sequence designs limited by selection rules, there is a qutrit interaction decoupling sequence based on unitary 2-designs and the Clifford group in our complementary work [72], which is theoretically elegant but not practical experimentally because it requires driving on all three transitions.

To overcome this challenge and the previous point (i.e., the lack of a Bloch sphere picture), we propose the concept of "decoupling frame graphs," which keeps track of the connectivity between frames using experimentally implementable pulses (see Sec. III B for detailed discussions). A decoupling frame graph not only labels all pairs of frames that can be directly connected using available controls but also organizes the frames in a structured way, similarly to the qubit Bloch sphere, and thereby serves as the backbone on which pulse sequences are designed.

D. Complicated trajectories of frames during pulses

In order to build in robustness against dynamics during the finite pulse duration and possible rotation angle errors coming from miscalibration or Rabi inhomogeneity, one must know the frame $\tilde{S}^z$ during the pulses because it determines the transformation of $\tilde{H}$. In the qubit case, this task is easy: We can see from the Bloch sphere picture that, during any $\pi/2$ pulse rotation,

$$\tilde{S}^z(\theta) = S_1 \cos\theta + S_2 \sin\theta, \tag{2}$$

where $S_{1/2}$ are the frames before and after the $\pi/2$ pulse and θ represents the time during the pulse. Thus, the whole trajectory during the pulse is conveniently represented as a linear combination of the discrete frames before and after the pulse. With this exact and simple expression, the effect of control imperfections can be calculated analytically, which enables the design of pulse sequences robust to them [17].

In the qudit case, however, the trajectories during pulses can be very complicated due to the higher (i.e., d^2-1) dimension of the operator space. For example, in the qutrit case, the frame trajectory lives in a six-dimensional space during a generic pulse, which makes the instantaneous frames completely untractable (see Appendix B 4). In fact, even for relatively simple pulses, such as a $\pi/2$ pulse on a single transition, no decomposition like Eq. (2) is possible, as discussed in Appendix B 4.

To overcome this challenge, we identify special conditions under which Eq. (2) continues to hold in the qudit case: The pulse needs to transform frames along geodesics on the generalized Bloch sphere [22,67]. Remarkably, such geodesic-generating pulses only involve transitions between neighboring $|m_S\rangle$ states, which satisfy the selection rules in most cases. See Sec. III C for detailed discussions.

The challenges discussed above make qudit sequence design substantially harder than the qubit case. It should be clear from the preceding discussion that a better understanding of the underlying structure of the qudit sequence design problem is necessary to facilitate their design. Our work develops a formalism that identifies and captures this structure, thereby providing a general recipe for robust qudit sequence design.

III. GENERAL FORMALISM FOR QUDIT HAMILTONIAN ENGINEERING

In this section, we introduce our general formalism for robust qudit Hamiltonian engineering. Key to our formalism are insights into compact algebraic and graphical representations of the engineered Hamiltonian, combined with judicious choices of pulse families to satisfy real-world constraints and achieve robustness. Many of these observations are inspired by methods for robust qubit sequence design, yet require viewing the results from a new perspective and making substantial generalizations. For a more detailed description of robust qubit sequence design, we refer the reader to Ref. [17].

In each subsection below, we first illustrate the intuitions behind key insights using simple examples with qubits and then generalize the statements to the qudit case. As we shall see, this is a nontrivial extension and requires developing new geometric intuitions and understandings of the Hamiltonian engineering constraints.

A. Hamiltonian representation and decoupling frame set

The setting we are interested in is a generic qudit Hamiltonian

$$H = \sum_i H_i^{\mathrm{dis}} + \sum_{i\neq j} H_{ij}^{\mathrm{int}}, \tag{3}$$

where the first term describes an on-site disorder and the second term describes a symmetric two-body interaction that satisfies the rotating wave approximation (i.e., the secular approximation). We focus on the case where we only have global control over the spin system, consisting of

pulses allowed by the selection rules of the system. Going into the interaction picture with respect to the ideal pulses, we can write the interaction picture Hamiltonian as $\tilde{H}_k = U_{k-1}^\dagger H U_{k-1}$, with $U_{k-1} = P_{k-1}\cdots P_1$. In average Hamiltonian theory, the evolution of the system can be described by an effective Hamiltonian H_{eff}, which is the average of $\tilde{H}_k$ weighted by the corresponding evolution times τ_k [26], $H_{\text{eff}} = \sum_k \tau_k \tilde{H}_k/T$, T being the Floquet period. The goal of Hamiltonian engineering is then to design a pulse sequence $\{P_k\}$ that leads to the desired form of H_{eff}.

As we discussed in Sec. II, the key insight that significantly simplifies the pulse-sequence design problem in the qubit case is that the Hamiltonian transformation $\tilde{H} = U^\dagger H U$ is uniquely determined by the frame transformation $\tilde{S}^z = U^\dagger S^z U$. This observation allows us to keep track of only the S^z transformation, instead of the whole unitary U or the pulse-sequence history, which contain unnecessary information about the transformations of S^x and S^y.

The fundamental reason for this insight is the rotating wave approximation (i.e., secular approximation). Intuitively, when there is a strong quantizing field that separates the two energy levels, the Hamiltonian rapidly rotates around the z axis. Therefore, any part of the Hamiltonian that is not rotationally invariant rapidly averages out, and the resulting Hamiltonian must be invariant under z rotations. Because of this, the rotation of the x and y axes in the plane perpendicular to the z axis does not matter, as they are equivalent, and the transformation of the z axis determines everything.

The observation that $\tilde{S}^z$ uniquely determines $\tilde{H}$ can be directly generalized into the higher spin case, and we formulate this statement precisely as the following theorem:

Theorem 3.1. For two unitaries U_1, U_2, such that $\tilde{S}^z = U_1^\dagger S^z U_1 = U_2^\dagger S^z U_2$, we have $(U_1^\dagger)^{\otimes n} H U_1^{\otimes n} = (U_2^\dagger)^{\otimes n} H U_2^{\otimes n}$, where n is the number of spins in the system and H is a qudit Hamiltonian satisfying the secular approximation on each transition.

The full proof is given in Appendix A 3, but the basic intuition is similar to the spin-$\frac{1}{2}$ case: The rotating wave approximation causes operators other than diagonal ones to drop out, leaving $\tilde{S}^z$ as the only relevant information.

Since transformations of the S^z operator alone are sufficient to describe the Hamiltonian transformations, we only need to keep track of them for the Hamiltonian engineering problem. Compared to prior approaches that did not utilize the secularity of the Hamiltonian [22,54], Theorem 3.1 reduces the information we need to keep track of and makes it possible to extract physical insights from the frames $\tilde{S}^z$ themselves that help inform sequence design, as we shall see in Sec. IV.

The proof in Appendix A 3 does not provide an explicit construction of the transformed Hamiltonian as a function of $\tilde{S}^z$, although it is easy to show that the final result will be a polynomial in the decomposition coefficients of $\tilde{S}^z$ in the Gell-Mann basis, as we describe in Appendix A 4. The explicit form of the transformed Hamiltonian is rather complicated and is 4 pages long (Appendix A 6). Using the representation theory of Lie groups, such expressions can, in fact, also be directly constructed, as we show in complementary work [72].

B. Graphical representation of qudit decoupling

In this section, we introduce a new graphical representation, which we call the decoupling frame graph, to describe the frame set we use to decouple the interaction and the pulses connecting them. In these graphs [e.g., Figs. 3(b) and 3(e)], the vertices represent the frames we use for decoupling, and the edges represent the pulses connecting these frames. As we will discuss in this section, this graphical representation directly reflects the structure of the problem, significantly simplifying the inclusion of connectivity requirements while also providing a simple visualization of the pulse sequence.

To make Hamiltonian engineering techniques relevant to real-world experiments, the key is to ensure that the desired transformations can indeed be experimentally implemented given the constraints of selection rules. To build in robustness into a pulse sequence, the pulses connecting neighboring frames must be simple enough that we can easily analyze the effects of disorder and interaction during them. Therefore, we require neighboring frames to be connected by simple and experimentally implementable pulses.

For qubit systems, this requirement is automatically achieved through the Bloch sphere picture in Fig. 3(a), where the frames $\pm S^x, \pm S^y, \pm S^z$ are connected by simple $\pi/2$ pulses. Generalizing this to the qudit case would require us to keep track of the connectivity between relevant frames and to build a graph similar to Fig. 3(b), where vertices represent the frames and edges represent connectivity between them. However, it is not obvious that such a representation is even well defined because, depending on the pulse history, there could be multiple different unitaries U_i leading to the same frame $\tilde{S}^z = U_i^\dagger S^z U_i$ while the other omitted information (i.e., $\tilde{S}^x$ and $\tilde{S}^y$) is different. Therefore, one may generically expect that the connectivity from one frame to another frame may depend on which underlying unitary is used to realize the first frame.

To see this subtle point more clearly, let us consider a simple qubit example. The frame S^z may come from two different unitaries: The first one is the trivial identity $U_1 = I$, and the second one is a rotation by $\pi/2$ around the Z axis, $U_2 = \mathrm{e}^{-i\frac{\pi}{2}S^z}$, which rotates the Z axis into itself. In order to reach the frame S^x from these two unitaries that both lead to the S^z frame, one actually needs to apply a $\pi/2$ pulse around $-Y$ in the first case and a $\pi/2$ pulse around $+X$ in the second case. Therefore, the specific pulse

required to go from one frame to another frame may depend on the details of the pulse history, and there is no guarantee that all these different pulses would satisfy the selection rules in the qudit case. Fortunately, as we state precisely in the following theorem, we find that all these different pulses can only differ by the phase of the driving on each transition, which does not change the implementability under the selection rules.

Theorem 3.2. For two unitaries U_1, U_2 leading to the same frame $\tilde{S}^z = U_1^\dagger S^z U_1 = U_2^\dagger S^z U_2$ and a pulse U_P that transforms the first case to $\tilde{S}^z_{\text{new}} = U_1^\dagger U_P^\dagger S^z U_P U_1$, there exists a diagonal phase operator U_{phase}, such that the phase-shifted pulse $U_{P'} = U_{\text{phase}}^\dagger U_P U_{\text{phase}}$ transforms the second case to the same frame $\tilde{S}^z_{\text{new}} = U_2^\dagger U_{P'}^\dagger S^z U_{P'} U_2$.

The proof of the theorem is given in Appendix A 5. Given Theorem. 3.1, stating that the only thing we need to keep track of is the frame $\tilde{S}^z$, and Theorem. 3.2, stating that the connectivity between the frames is well defined, the structure of the whole problem can be naturally incorporated in the graphical representation in Fig. 3, where vertices represent the frames that dictate the transformed Hamiltonian and edges represent experimentally implementable pulses connecting those frames. We refer to this representation as the decoupling frame graph. A pulse sequence can then be represented as a path on this graph, with the decoupling requirement $H_{\text{eff}} = \sum_k \tilde{H}_k \tau_k = 0$ becoming a requirement on the frame set and the time τ_k spent at each vertex. We emphasize that the decoupling frame graph plays a similar role to the missing Bloch sphere picture [see Figs. 3(b) and 3(e)], which encodes the adjacency of relevant frames and serves as the backbone for pulse-sequence designs.

To build a decoupling frame graph, one starts with a simple pulse set motivated by selection rules and easy analysis of robustness (Sec. III C). One then applies the pulses a few layers deep to generate a set of frames accessible using these pulses. Crucially, one should also keep track of how the different frames are connected by pulses in the chosen pulse set in this process and generate an overcomplete decoupling frame graph in which not every vertex is necessarily needed. Finally, one applies the linear programming techniques described in Ref. [22] on the set of frames generated (instead of on all possible unitaries in the existing methods) to identify a subset of frames and weights that achieve decoupling. The subset of frames and the connectivity between them gives the decoupling frame graph on which we design pulse sequences.

Two comments are in order: First, when there are multiple solutions to the linear programming question when choosing the subset of frames, frames connected in a single patch are more favorable because this eliminates the need for intermediate vertices to connect frames, which could complicate the cancellation of finite-pulse-duration effects. Similarly, well-connected graphs are preferred because they support more ways to traverse the vertices. This extra degree of freedom can be utilized to satisfy the robustness conditions. Second, the choice of a well-motivated, implementable set of pulses is very important, as it determines the frames we consider and the connectivity between them. As we will see in Sec. III C, balanced double-driving pulses (i.e., pulses that simultaneously drive both $|0\rangle \leftrightarrow |+1\rangle$ and $|0\rangle \leftrightarrow |-1\rangle$ transitions with equal amplitude) are usually good choices in spin-1 systems due to their simple transformations of disorder during pulses and their ease of implementation and calibration.

Let us now provide a few concrete examples of the decoupling frame graph to gain a bit more intuition.

First, consider the qubit case, where we would like to spend equal time along each of the six cardinal directions. The vertices thus correspond to $\pm S^x$, $\pm S^y$, $\pm S^z$ frames, and the connecting edges, corresponding to $\pi/2$ pulses, organize the decoupling frame graph into an octahedron, as shown in Fig. 3(b). A representative path on this graph can then be directly translated into the decoupling pulse sequence shown in Fig. 3(c). This sequence is a variant of the spin-1/2 WAHUHA sequence that decouples interactions and disorder [20].

Another decoupling frame graph, which we use for qutrit disorder and interaction decoupling, is shown in Fig. 3(e). The definition of the frames and why it decouples disorder and interactions is discussed in Sec. IV; for now, however, it is just an illustration of a generic qudit decoupling frame graph. Similar to the qubit case, we can easily draw a path through all vertices in a simply connected fashion. The pulse sequence corresponding to the path is shown in Fig. 3(f) and consists of balanced double-driving pulses with different phases on each transition.

C. Robust qudit decoupling

In order to incorporate robustness into sequence design, we have to analyze the transformation of the Hamiltonian during pulses. For qudit systems, the transformation trajectory can be much more complex than the qubit case (see below and Appendix B 4), complicating the robustness analysis. Nevertheless, we will show that, by carefully choosing the pulses that constitute the sequence, we can recover the favorable properties of the qubit case.

Before diving into the more complicated case of qudits, let us first briefly review how disorder during pulses is canceled in the qubit case in order to remind readers about the key properties that simplify the analysis. Because the on-site disorder is proportional to S^z, we need to analyze the transformation of the S^z operator during pulses. In the qubit case, the transformation of the S^z operator during pulses is a continuous rotation along a geodesic on the Bloch sphere from the frame before the pulse S_1 to the frame after the pulse S_2. If we focus on the two-dimensional subspace that contains the trajectory of $\tilde{S}^z$ during the pulse, this trajectory is represented by the red arc

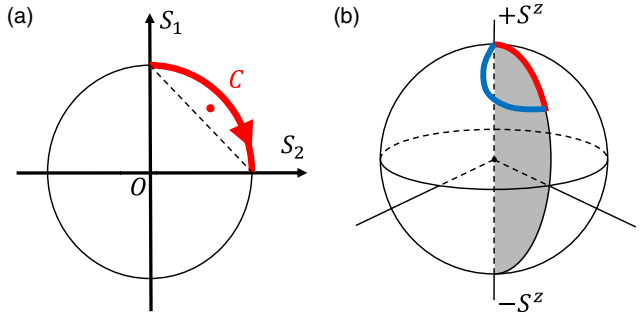

FIG. 4. Disorder during pulses. (a) In the qubit case, the disorder during pulses is a continuous rotation from the frame before the pulse S_1 to the frame after the pulse S_2, as represented by the red arc. Therefore, its average effect, which is represented by the center of mass "C" of the red arc, can be written as a scaled average of S_1 and S_2. The factor $4/\pi$ in Eq. (4) comes from the fact that the center of mass C is slightly further from the origin compared to the midpoint of S_1 and S_2. (b) Illustration of geodesics. If the trajectory of S^z during the pulse follows a geodesic, as in the case of the red curve, then the whole curve lives in the two-dimensional subspace (i.e., the shaded plane) spanned by the frame before and after the pulse, and therefore the average effect of disorder during the pulse can naturally be decomposed as an average before and after the pulse. If the trajectory of S^z does not follow a geodesic, as in the case of the blue curve, then the center of mass of the curve no longer lives in the shaded plane and no such decomposition is possible.

in Fig. 4(a). Therefore, the average effect of disorder during the pulse, which is represented by the center of mass of the red arc, can be decomposed as a simple average of S_1 and S_2. Indeed, by integrating over the pulse explicitly, one finds that the average effect of disorder during a $\pi/2$ pulse is

$$\overline{S} = \frac{4}{\pi}\left[\frac{S_1 + S_2}{2}\right]. \tag{4}$$

The contributions of these terms can be easily incorporated into the effective Hamiltonian by treating it as extra time spent in the frames before and after the pulse, with minimal changes to the decoupling conditions otherwise. Thus, in the qubit case, this decomposition significantly simplifies the incorporation of robustness into the sequence design problem. For more details on qubit robust sequence design and a similar analysis of other contributions, we refer readers to Ref. [17].

However, this decomposition of disorder during pulses as a simple average before and after the pulse no longer holds for generic pulses in the qudit case. A concrete counterexample is the transformation of the spin-1 S^z operator during a $\pi/2$ pulse applied on a single transition, which is discussed in more detail in Appendix B 4. A geometric picture that explains why this decomposition [i.e., Eq. (4)] no longer holds is that the trajectory of the S^z transformation during pulses is no longer a geodesic on the generalized Bloch sphere [22,67] for generic higher spin pulses. To see the effect of this case, examine Fig. 4(b), where the red curve represents a trajectory of $\tilde{S}^z$ that follows a geodesic and the blue curve is a trajectory that does not follow a geodesic. For the red curve, since it lives entirely in the two-dimensional subspace spanned by $\tilde{S}^z$ before and after the pulse (i.e., the shaded plane), the averaged $\tilde{S}^z$ during the pulse can always be decomposed as a scaled average of $\tilde{S}^z$ before and after the pulse. However, for the blue curve, since its center of mass does not live in the shaded plane, there is no way to perform this decomposition.

One way to overcome this challenge is to find pulses that transform S^z along geodesics and use them to build the decoupling sequence. For the case of a spin-1 system, we find that balanced double-driving pulses (i.e., pulses that simultaneous drive both $|0\rangle \leftrightarrow |+1\rangle$ and $|0\rangle \leftrightarrow |-1\rangle$ transitions with equal amplitude) satisfy this condition. For concreteness, let us write down the form of the Hamiltonian for balanced double-driving pulses:

$$H_p \propto \begin{pmatrix} 0 & e^{-i\theta_1} & 0 \\ e^{i\theta_1} & 0 & e^{-i\theta_2} \\ 0 & e^{i\theta_2} & 0 \end{pmatrix}. \tag{5}$$

To see that balanced double-driving pulses transform S^z along geodesics, notice that the Hamiltonian of balanced double-driving pulses can be related to the spin-1 S^x operator by a simple conjugation $H_p = U^\dagger S^x U$, where the unitary

$$U = \begin{pmatrix} e^{i\theta_1} & 0 & 0 \\ 0 & 1 & 0 \\ 0 & 0 & e^{-i\theta_2} \end{pmatrix} \tag{6}$$

is a phase operator that conjugates the S^z operator trivially (i.e., $U^\dagger S^z U = S^z$). Then, the transformation of the S^z operator during the pulse is

$$\begin{aligned} \tilde{S}^z(t) &= e^{iH_p t} S^z e^{-iH_p t} \\ &= U^\dagger [e^{iS^x t} S^z e^{-iS^x t}] U. \end{aligned} \tag{7}$$

Notice that the term $e^{-iS^x t}$ is a spin-1 spatial rotation operator, so its conjugation on S^z transforms S^z along the geodesic $\cos t S^z + \sin t S^y$. This property still holds after conjugation by U, and we find that, for arbitrary balanced double-driving pulses that rotate the spin by $\pi/2$, the transformation of S^z during the pulse is a geodesic:

$$\tilde{S}^z(\theta) = \cos\theta S_1 + \sin\theta S_2, \tag{8}$$

where $S_{1,2}$ are the frames before and after the pulse and θ is the angle rotated from S_1. We remark that the above

constructions and proof can be generalized to qudits with arbitrary d, where the balanced double driving is generalized to a phase-conjugated higher spin S^x operator. Furthermore, such pulses are implementable in most experimental systems because they only require driving between neighboring $|m_S\rangle$ states.

Equation (8) shows that, by using pulses that transform S^z along geodesics in qudit sequence design, we achieve exactly the same transformation of S^z as in the qubit case. This finding significantly simplifies the robustness condition analysis, and as we will discuss in Sec. IV, it allows us to cancel other terms, including disorder that is proportional to $(S^z)^2$, rotation angle errors, and dominant higher-order contributions, by analogy with the qubit case. For a more detailed analysis of robustness conditions, see Appendixes B 4 and B 5.

D. General recipe for robust qudit sequence design

Combining the preceding insights, we arrive at the following prescription for designing qudit robust Hamiltonian engineering sequences:

(1) Choose a fixed set of physically implementable pulses; ideally ones that cause frame trajectories along geodesics.
(2) Apply the pulses a few layers deep to build a decoupling frame graph, where edges correspond to the pulses chosen above and vertices are frames $\tilde{S}^z$ accessible using pulses in the chosen pulse set.
(3) Apply linear programming techniques described in Ref. [22] to identify a subset of frames and weights that achieve decoupling.
(4) Identify a path on the decoupling frame graph that walks through all desired frames, spends the required time at each vertex, and cancels the evolution during pulses. This is usually achievable if we choose a pulse set that transforms S^z along simple trajectories (e.g., geodesics) in step 1.

The end result will be an experimentally implementable decoupling sequence that decouples both disorder and interactions and is robust to various control imperfections. We note that some of these conditions can be relaxed. For example, even if the pulses do not exclusively result in geodesic precessions, we can still perform robust Hamiltonian engineering through careful design, as described in Appendix B 7.

IV. DESIGNING A GOOD QUTRIT DECOUPLING SEQUENCE

In this section, we use the general recipe described in Sec. III D to design a robust disorder and interaction decoupling sequence for a dipolar interacting spin-1 ensemble. The Hamiltonian of the system we are considering is

$$H = \sum_i [h_i S_i^z + D_i (S_i^z)^2] + \sum_{ij} J_{ij} \left[S_i^z S_j^z - \frac{1}{2} H_{ij}^{XY,0+} - \frac{1}{2} H_{ij}^{XY,0-} \right], \quad (9)$$

where the first term describes two independent modes of the on-site disorder, which we call "S^z disorder" and "$(S^z)^2$ disorder" from now on, and the second term is the dipole-dipole interaction after applying RWA. The symbol $H_{ij}^{XY,0+}$ in the second term is shorthand for the flip-flop term $H_{ij}^{XY,0+} \equiv |+1,0\rangle\langle 0,+1| + \text{H.c.}$ between $|0\rangle$ and $|+1\rangle$, and the symbol $H_{ij}^{XY,0-}$ is a similar flip-flop term between $|0\rangle$ and $|-1\rangle$.

Now, let us design a robust disorder and interaction decoupling sequence using this general recipe. We choose to work with balanced double-driving pulses because they transform S^z along geodesics. By a linear programming search on the accessible frames, which is described in more detail in Ref. [22] and Appendix B 1, we find that the 12 frames in Fig. 3(d) constitute a decoupling frame set when we spend equal time on each vertex. The explicit expressions of these frames are

$$\pm S^x = \pm\frac{1}{\sqrt{2}}\begin{pmatrix} 0 & 1 & 0 \\ 1 & 0 & 1 \\ 0 & 1 & 0 \end{pmatrix}, \quad \pm S^{\tilde{x}} = \pm\frac{1}{\sqrt{2}}\begin{pmatrix} 0 & 1 & 0 \\ 1 & 0 & -1 \\ 0 & -1 & 0 \end{pmatrix},$$
$$\pm S^y = \pm\frac{1}{\sqrt{2}}\begin{pmatrix} 0 & -i & 0 \\ i & 0 & -i \\ 0 & i & 0 \end{pmatrix}, \quad \pm S^{\tilde{y}} = \pm\frac{1}{\sqrt{2}}\begin{pmatrix} 0 & -i & 0 \\ i & 0 & i \\ 0 & -i & 0 \end{pmatrix},$$
$$\pm S^z = \pm\begin{pmatrix} 1 & 0 & 0 \\ 0 & 0 & 0 \\ 0 & 0 & -1 \end{pmatrix}, \quad \pm S^{\tilde{z}} = \pm\begin{pmatrix} 0 & 0 & -i \\ 0 & 0 & 0 \\ i & 0 & 0 \end{pmatrix}. \quad (10)$$

The next step is to build in robustness by choosing a good path on the decoupling frame graph. In order to build a high-performance decoupling sequence, in addition to the robustness conditions, it is also crucial for the dominant terms in the Hamiltonian to be canceled as locally as possible to avoid generating a large higher-order contribution in the Magnus expansion [73]. Therefore, the overall design principle involves a hierarchical structure: Shorter sequences are designed to robustly cancel the dominant terms in the Hamiltonian, and they are used as building blocks for longer sequences that cancel the subdominant terms.

In our experimental platform consisting of a dense NV ensemble, the ordering of energy scales in the Hamiltonian (from large to small) is magnetic noise ($\propto S^z$), electric field noise and strain inhomogeneities [$\propto (S^z)^2$], and the dipole-dipole interaction, and we also aim to cancel them in this order in our pulse sequence. We note that different

experimental platforms can have different relative magnitudes of these terms, and the hierarchical design method we discuss in this section should still lead to good pulse sequences in those cases.

Let us now describe the hierarchies from the lowest level to the highest level.

A. Cancel magnetic noise S^z

Since magnetic noise is the dominant term in our platform, it is canceled on the lowest level in the pulse-sequence hierarchy. The basic structure to cancel the magnetic noise is shown in Fig. 5(a). In these plots, we represent the pulse sequence by a frame matrix, where each column describes a frame and each row represents a basis vector we use to decompose the frames. The frames are represented by their decomposition coefficients in this basis; for example, a "+1" in the row corresponding to S_2 denotes the frame $+S_2$, and a "−1" in the S_1 row denotes the frame $-S_1$. The square blocks in these plots represent free evolution periods between pulses, and the thin lines represent intermediate frames that we go through during pulses. For a more detailed description of these plots in the qubit case, see Ref. [17]. In Fig. 5(a), there is a pair of square blocks $+S_2$ and $-S_2$, so the S^z disorder during free evolution is canceled; in addition, there is a pair of thin lines $-S_1$ and $+S_1$, so the S^z disorder during pulses is also canceled. Therefore, this basic structure cancels S^z disorder robustly, and we will use it as the building block for higher-level sequences that cancel other terms in the Hamiltonian.

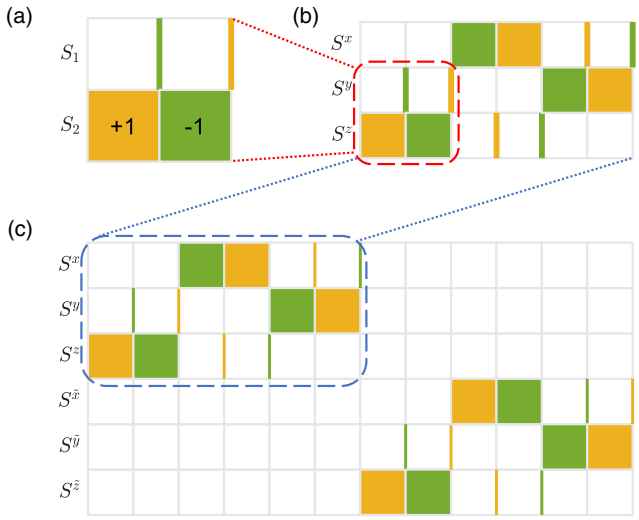

FIG. 5. Hierarchy of sequences. (a) Basic building block we use to cancel S^z disorder. Here, S_1 and S_2 represent two generic frames connected by microwave pulses, and yellow and green represent the signs $+S_{1,2}$ and $-S_{1,2}$, respectively. The large square blocks indicate free evolution between pulses, and the thin lines indicate intermediate frames during pulses (e.g., the thin green line in the S_1 row indicates a π pulse from S_2 to $-S_2$ that goes through $-S_1$). Notice that disorder during both free evolution and pulses is canceled. (b) A WAHUHA-like sequence built by the building blocks in diagram (a), which cancels the $(S^z)^2$ disorder. (c) A sequence that decouples both disorder and interactions, obtained by applying the WAHUHA sequence in diagram (b) on each block in Fig. 6.

B. Cancel electric field and strain noise $(S^z)^2$

The next level in the hierarchy is canceling electric field noise and strain inhomogeneities. An important observation here is that the WAHUHA sequence [20], which is designed to cancel spin-$\frac{1}{2}$ XXZ interactions, can also cancel the spin-1 $(S^z)^2$ disorder. Specifically, consider a spin-1 version of the WAHUHA sequence that goes through the frames S^x, S^y, and S^z, where $S^{x,y,z}$ are conventional spin-1 operators (see above). The reason that this sequence cancels the $(S^z)^2$ disorder is because it transforms the disorder into $(\hat{S}^x)^2 + (\hat{S}^y)^2 + (\hat{S}^z)^2 = \hat{S}^2 = S(S+1)\mathbb{1} \propto \mathbb{1}$, which is a trivial constant. Moreover, because of the similar structure of $(\hat{S}^z)^2$ and the spin-$\frac{1}{2}$ interaction $\hat{S}^z \otimes \hat{S}^z$, both being quadratic in S^z, their contribution during the finite pulse can be canceled using the same method, as discussed in more detail in the fourth level of the hierarchy and in Ref. [17]. In addition, we find that the 12 frames in Fig. 3(d) can be divided into two blocks of six frames (as shown in Fig. 6), in which the frames in each block $(\pm\hat{S}_1, \pm\hat{S}_2, \pm\hat{S}_3)$ satisfy $\hat{S}_1^2 + \hat{S}_2^2 + \hat{S}_3^2 \propto \mathbb{1}$, achieving the same cancellation as above. Therefore, we can cancel the $(S^z)^2$ disorder locally by applying a WAHUHA sequence on each block, as shown in Fig. 5(b). Note, however, that a WAHUHA sequence does not fully cancel the $(S^z)^2$ disorder during the finite pulse duration, and we postpone this cancellation to the fourth level.

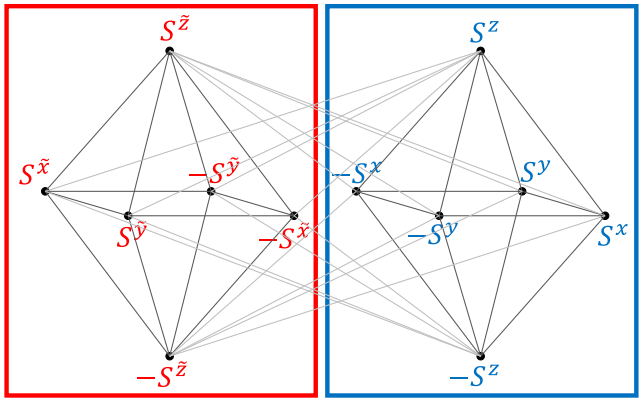

FIG. 6. Dividing the 12 frames into two pseudo-Bloch spheres. The six frames in each pseudo-Bloch sphere $(\pm\hat{S}_1, \pm\hat{S}_2, \pm\hat{S}_3)$ satisfy $\hat{S}_1^2 + \hat{S}_2^2 + \hat{S}_3^2 \propto \mathbb{1}$; therefore, a WAHUHA sequence in each pseudo-Bloch sphere cancels the $(S^z)^2$ disorder. We emphasize that the observation of such a simplification heavily relies on the geometric insights provided by the decoupling frame graph.

C. Cancel dipole-dipole interactions

The third level in the hierarchy is to cancel the dipole-dipole interaction. As we found from our linear programming analysis in Sec. III B, this process requires us to spend equal time in all 12 frames in Fig. 6 and is achieved by concatenating the WAHUHA sequences on the two blocks in Fig. 6. The frame representation of this sequence is shown in Fig. 5(c).

D. Further improvements inspired by advanced qubit sequence design

Inspired by recent advances in qubit higher-order sequence design [74] and the similarity between certain terms in qutrit decoupling and qubit decoupling, we can use the interaction decoupling sequence shown in Fig. 5(c) as a building block and apply the higher-order designs in Ref. [74] to further improve its performance. Phenomenologically, we repeat the sequence in Fig. 5(c) 8 times while flipping the signs and ordering of the frames in each repetition, as shown in Fig. 14(a). The combination of these different sign and ordering choices further cancels the residual $(S^z)^2$ disorder during the pulses, the Rabi inhomogeneity effect, and dominating higher-order terms in the Magnus expansion coming from commutators between various terms (see Ref. [74] for detailed discussions), and leads to better decoupling performance. We emphasize that the decoupling frame graph plays an important role in this process: It provides graphical insights that help one easily reason about possible variants of the sequence in Fig. 5(c) and combine multiple variants to symmetrize the trajectory on the decoupling frame graph. A numerical comparison of sequences with different levels of symmetrization is shown in Fig. 19.

As an example, the $(S^z)^2$ disorder during the pulses and the Rabi inhomogeneity effect are canceled by flipping the signs of the intermediate frames (or the free evolution frames, but not both) in the basic building block shown in Fig. 5(a). The cancellation of $(S^z)^2$ disorder during pulses relies on the fact that it transforms in the same way as spin-$\frac{1}{2}$ Ising interactions. Specifically, if we denote the frame before and after a spin-1 $\pi/2$ pulse by S_1 and S_2 and denote the angle rotated from S_1 by θ, then the instantaneous frame is $\cos\theta S_1 + \sin\theta S_2$ (see Sec. III C for the derivation). The $(S^z)^2$ disorder is thus transformed to $\cos^2\theta S_1^2 + \sin^2\theta S_2^2 + \sin\theta\cos\theta(S_1S_2 + S_2S_1)$. The terms proportional to S_1^2 and S_2^2 can be viewed as additional time spent in the frame right before and right after, and therefore are canceled by the WAHUHA block itself. The cross term $S_1S_2 + S_2S_1$ is canceled here because one of S_1 and S_2 is an intermediate frame whose sign is flipped, in analogy to the rule for interaction cross terms in Ref. [17]. Meanwhile, the Rabi inhomogeneity effect is canceled because the rotation direction changes when the sign of one frame in S_1 and S_2 is flipped, leading to forward and backward rotations that compensate each other, in direct analogy to the chirality sum rule in Ref. [17]. Because of this robust design, the sequence performance is not very sensitive to a slight miscalibration of the rotation angle, despite the sequence involving as many as 100 pulses. Furthermore, by a similar analysis, one can show that the final sequence is not only robust to rotation angle errors common to both transitions as discussed above, but it is also robust to rotation angle errors on each individual transition (see Appendix B 5 for details). Similar analogies to the qubit case also apply to higher-order contributions.

With the preceding hierarchical construction, we arrive at a set of promising decoupling pulse sequences, as described in full detail in Appendix B 2. For applications on other experimental platforms, the ordering of levels 1 to 3 in the hierarchy can be changed based on the relative magnitude of disorder and interactions; the symmetrizations in level 4 are optional based on the trade-off between better decoupling performance versus shorter sequence length, which is discussed in more detail in Appendix C 2.

V. QUTRIT DECOUPLING EXPERIMENT

We now test the performance of the robust qutrit decoupling sequence proposed in Sec. IV in a high-density ensemble of spin-1 NV centers in diamond [43,75], resulting in the first demonstration of full decoupling of qudit interactions. We isolate NVs with the same lattice orientation with an external magnetic field aligned with one group of NV centers. This magnetic field also breaks the degeneracy between energy levels $|\pm 1\rangle$, allowing us to address the transitions $|0\rangle \leftrightarrow |+1\rangle$ and $|0\rangle \leftrightarrow |-1\rangle$ separately, using microwaves with frequencies 3.647 GHz and 2.092 GHz, respectively. The density of NV centers along each lattice orientation in our sample is about 4 ppm, which corresponds to a typical interaction strength of $J = 2\pi \times 35$ kHz. The strength of the on-site S^z disorder and $(S^z)^2$ disorder is about $2\pi \times 4$ MHz and $2\pi \times 1$ MHz, respectively (Gaussian standard deviation). In the experiment, we optically initialize the state of NVs to be in $|0\rangle$, apply microwave pulses to prepare various initial states, then apply the decoupling sequence, and finally reverse the preparation sequence before reading out the population in state $|0\rangle$ via fluorescence differences (see Fig. 7 and Ref. [43] for more details).

The measured decay of the signal under various decoupling sequences is plotted in Fig. 8(a). Sequences with numerical labels are existing sequences from the literature, while the ones with alphabetical labels are new sequences we designed. Sequence 2 is the interaction decoupling sequence in Ref. [22]. Its performance in our experiment is not good because it does not decouple the disorder, which is the dominant term in our system. To cancel the disorder, we can use Seq. 1 from Ref. [66], which directly generalizes the spin-$\frac{1}{2}$ spin-echo sequence to the spin-1 case. Similarly to the spin-echo sequence, Seq. 1 only cancels disorder

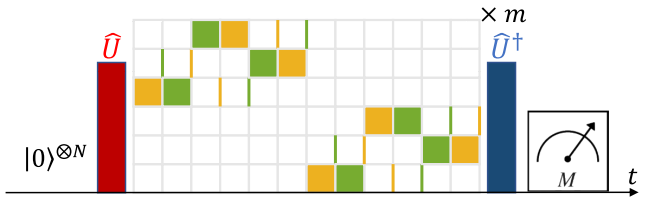

FIG. 7. Decoupling experiment. In the experiment, we first initialize the NVs to state $|0\rangle$ by shining a 532-nm green laser on our sample. We then apply the initialization microwave pulse $\hat{U}$ to prepare the initial state whose decay curve we want to measure. Next, the decoupling pulse sequence is applied, and finally, the preparation pulse is reversed before measuring the population in state $|0\rangle$.

during the free evolution, but it is not robust to disorder during pulses.

To improve the performance, we designed Seq. A, which is an enhanced version of Seq. 1 that is highly robust to disorder effects during pulses. This robust disorder decoupling sequence shows a significant timescale extension compared to its nonrobust counterpart, Seq. 1, highlighting the importance of robust sequence design. Furthermore, since Seq. A does not cancel interactions, it serves as a baseline for verifying interaction decoupling in further sequences. To decouple both the disorder and interaction, we designed Seq. B, which is the sequence shown in Figs. 3(e) and 3(f). Although this sequence further decouples the interaction, its performance in experiments is worse than Seq. A because it has no robustness built in. For a more detailed description of these sequences, see Appendixes B 2 and B 3.

Most importantly, after integrating all robustness considerations into the sequence design, we arrive at our current best sequence, Seq. C, which we call DROID-C3PO. This sequence decouples both disorder and interactions, and is robust to disorder during pulses, rotation angle errors, and dominant higher-order contributions. In the experiment, this sequence shows significant improvement over Seq. A, constituting the first demonstration of full disorder and interaction decoupling in a qudit system, and it achieves a tenfold improvement over the existing sequences. In addition, we verify in Fig. 8(b) that the decay timescales of all initial states are extended under Seq. C, confirming that this sequence is a true decoupling sequence that preserves an arbitrary quantum state. We note that some of the other sequences plateau at higher values in Fig. 8(a). This may originate from residual disorder, which can project the spin population onto the disorder axis and give rise to a long-lived signal. However, this does not affect our conclusion because the plateau values for other sequences are higher than those for DROID-C3PO, which can only cause an overestimation of those coherence times relative to DROID-C3PO. The complete plot of Seq. C is shown

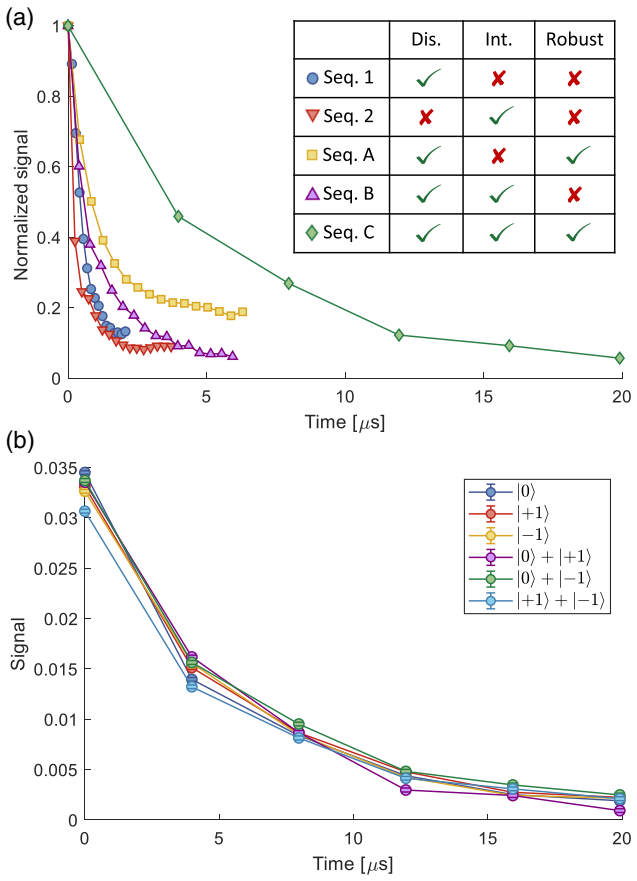

FIG. 8. Decoupling experiment results. (a) Measured average decay trace for different pulse sequences, where the average is taken over all three coherent superposition initial states $|0\rangle+|-1\rangle/\sqrt{2}$, $|0\rangle+|+1\rangle/\sqrt{2}$, and $|+1\rangle+|-1\rangle/\sqrt{2}$. Among the sequences, Seqs. 1 and 2 are existing sequences in Refs. [22,66], respectively, while Seqs. A–C are new sequences that we designed. The inset table shows whether or not a sequence decouples disorder and interactions, and whether it achieves robustness against disorder during pulses. For more details on these sequences, see Appendixes B 2 and B 3. The measurement is performed with a differential readout, where we rotate the population in each of the three states $|+1\rangle$, $|0\rangle$, and $|-1\rangle$ to state $|0\rangle$ before doing the fluorescence measurement. Denoting the measured fluorescence by I_+, I_0, and I_-, respectively, the signal on the vertical axis is defined as $S=\frac{3}{2}(2I_0-I_--I_+/I_0+I_-+I_+)$, which is proportional to $P_0-\frac{1}{3}$, where P_0 is the population in state $|0\rangle$. The experimental parameters are $(t_{\pi/2}=8\ \text{ns}, \tau=25\ \text{ns})$, where $t_{\pi/2}$ is the time duration of each spin-1 $\pi/2$ pulse and τ is the time spent in each frame. (b) Decay curve of different initial states for our best decoupling sequence DROID-C3PO (Seq. C), showing that the sequence preserves an arbitrary initial quantum state.

in Fig. 1(b), and its frame matrix representation is shown in Fig. 14(a). The remaining decoherence under Seq. C is discussed in Appendix C 1, and the possibility for adding more observational windows in addition to integer numbers of Floquet periods is discussed in Appendix C 2.

VI. MANY-BODY PHYSICS: QUANTUM MANY-BODY SCARS

The same techniques developed above can also be used to engineer a rich family of interesting many-body Hamiltonians, which enables new phenomena not accessible in spin-$\frac{1}{2}$ systems. As a specific example, we will discuss the engineering of a Hamiltonian that supports quantum many-body scars—exotic nonthermalizing eigenstates embedded in an otherwise thermal spectra, which constitute a new class of thermalization phenomena in between thermalizing systems and many-body localized systems [32,76–84].

A recent paper [32] proposed that the bipartite spin-1 XY model naturally realizes quantum many-body scars. Specifically, the model contains two groups of spin-1 particles with no intragroup interactions but with intergroup $XX+YY$ interactions. The Hamiltonian for this model is given by

$$H=\sum_{i\in A,j\in B}J_{ij}\left(S_i^xS_j^x+S_i^yS_j^y\right)+h\sum_{i\in A,B}S_i^z, \tag{11}$$

where spins i and j reside in different groups A and B in the first term, and h is an external magnetic field coupled to S^z.

In this particular example, the scar subspace is formed by acting with raising operators, which act only on the $|+1\rangle,|-1\rangle$ subspace. More concretely, for the bipartite spin-1 XY model we are considering, we can define the SU(2) algebra operators:

$$J^{\pm}=\frac{1}{2}\sum_i a_i(S_i^{\pm})^2,\qquad J^z=\frac{1}{2}\sum_i S_i^z, \tag{12}$$

where $a_i=1/-1$ for spins in group A/B, and $S_i^{\pm},S_i^z$ are spin-1 raising, lowering, and S^z operators. With this notation, the eigenstates

$$|\mathcal{S}_n\rangle\propto(J^+)^n|-1\rangle^N \tag{13}$$

form the nonthermalizing scar manifold according to Ref. [32], where $|-1\rangle^N$ is the state with all spins fully polarized into $|-1\rangle$ and N is the total number of spins in the two groups. At the same time, the Hamiltonian itself does not commute with the subspace SU(2) generator $J^{\pm}$, indicating that it is not integrable. Indeed, one can verify that this Hamiltonian has a thermal spectrum [32], where generic initial states thermalize. Thus, the spin-1 XY model constitutes a quantum many-body scar.

Using our techniques, the bipartite spin-1 XY model discussed above can be engineered from the native dipole-dipole interaction in high-density NV-center samples. Here, the two groups in the model can be realized as NV centers along two lattice orientations, where the transition frequencies of the two groups are spectrally resolved and the two groups can be controlled independently. The intragroup interaction can be canceled by applying the robust interaction decoupling sequence in each group as discussed above. To engineer the intergroup XY interaction, notice that the two groups of NV centers along different lattice orientations are not on resonance with each other when an external magnetic field is applied. Therefore, the interaction between NVs residing in different groups is an Ising interaction $S^z\otimes S^z$. Thus, a simple way to engineer the intergroup XY Hamiltonian is to repeat the basic sequence twice and, in the second iteration, flip the signs of the frame pairs $\{\pm S^z,\pm S^{x'},\pm S^{y'},\pm S^{z'}\}$ on the second group of NVs while leaving the signs of the frame pairs $\{\pm S^x,\pm S^y\}$ unchanged (see Fig. 9). In this way, the $-S^zS^z,-S^{x'}S^{x'}$, $-S^{y'}S^{y'},-S^{z'}S^{z'}$ interactions in the second iteration cancel with the $+S^zS^z,+S^{x'}S^{x'},+S^{y'}S^{y'},+S^{z'}S^{z'}$ interactions in the first iteration, while the $+S^xS^x,+S^yS^y$ interactions in both iterations add up and give the desired XY Hamiltonian. A frame representation of the pulse sequence that engineers the scar Hamiltonian is shown in Fig. 9.

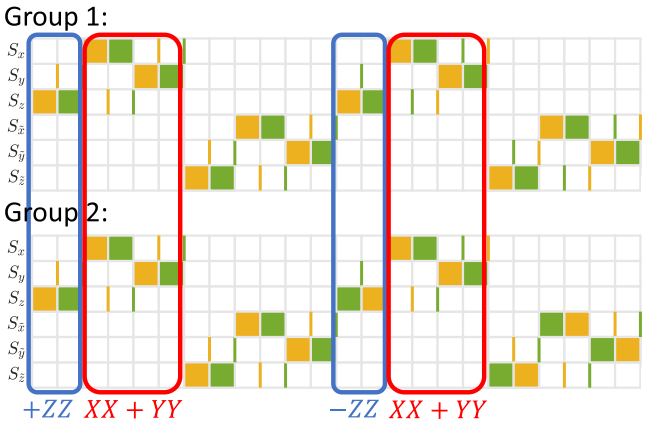

FIG. 9. Sequence engineering the scar Hamiltonian. The whole sequence to engineer the scar Hamiltonian $H=\sum_{i\in A,j\in B}J_{ij}(S_i^xS_j^x+S_i^yS_j^y)$ is plotted. Note that all intragroup interactions are decoupled by applying a decoupling sequence on each group individually and that, because of the sign flip in the second half of the sequence for group 2, all intergroup interactions are canceled (see blue boxes) except the S^xS^x and S^yS^y terms, which add up (see red boxes) and give the desired bipartite spin-1 XY model.

We simulate the dynamics of various initial states under this pulse sequence. The simulated initial states include $[(|+1\rangle+|-1\rangle)/\sqrt{2},(|+1\rangle-|-1\rangle)/\sqrt{2}]$, $[|+1\rangle,|+1\rangle]$, $[(|+1\rangle+|-1\rangle)/\sqrt{2},(|+1\rangle+|-1\rangle)/\sqrt{2}]$, $[|+1\rangle,|-1\rangle]$, $[|0\rangle,|0\rangle]$, where the first state in the brackets represents the initial state of the first group of spins and the second state in the brackets represents the initial state of the second group of spins. Based on the geometric intuition discussed in Appendix B 6 (which states that the scar subspace $|S_n\rangle$ is the maximal spin subspace after rotating the second group of spins by π around the z axis), the first two states live in

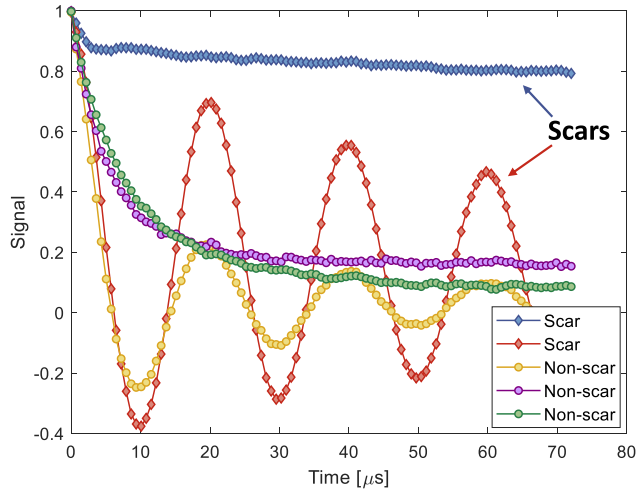

FIG. 10. Numerical simulation of the scar dynamics under the sequence in Fig. 9. We simulate the dynamics of various initial states under the sequence that engineers the scar Hamiltonian [Eq. (11)]. The experiment we simulated is the same type of experiment (i.e., initialize, evolve, readout) as in Fig. 7. The simulation parameters are ($\Delta = 0$, $J = 2\pi \times 35$ kHz, $h = 2\pi \times 25$ kHz, $t_{\pi/2} = 5$ ns, $\tau = 20$ ns, $N_1 = N_2 = 4$), where Δ is the disorder strength, $t_{\pi/2}$ is the time duration of each $\pi/2$ pulse, τ is the free evolution time spent in each frame, and N_1, N_2 are the number of spins in the two groups.

the scar subspace and therefore are not expected to thermalize, while the last three states do not live in the scar subspace and are expected to thermalize. The simulated dynamics of these initial states is plotted in Fig. 10. In the plot, we see that the initial states living in the scar subspace do not thermalize (their signal either stays large or has persistent oscillations), while the signals for other initial states quickly decay away. These results show that exotic quantum many-body scar states can be observed even in highly disordered, natural systems such as randomly positioned ensembles of NVs, in contrast to the more regular, clean systems in which they have been observed to date [76–78].

VII. ENHANCED QUANTUM SENSING WITH QUDIT HAMILTONIAN ENGINEERING

In addition to a rich landscape of many-body Hamiltonians, higher spin systems also give rise to interesting opportunities in quantum sensing. First, the higher spin implies a larger effective dipolar moment, which can lead to a linear or quadratic enhancement in magnetic field sensitivity, depending on the nature of the signal [85]. A well-known example of this for noninteracting spins is the use of double-quantum magnetometry for nitrogen-vacancy centers [38–40,86], and interacting spin systems present further challenges and opportunities for sensing sequence design [75,87]. Second, the larger Hamiltonian design space may also enable full time reversal of the interaction Hamiltonian, useful for entanglement-enhanced sensing [41,88], which may not otherwise be accessible with a subset of levels [43]. For example, the spin-1 dipolar interaction Hamiltonian projected onto $|0\rangle$ and $|+1\rangle$ has a nonzero trace when expressed in the Pauli basis, resulting in a Heisenberg interaction component that cannot be reversed through global drives; however, the full spin-1 dipolar interaction can nevertheless be fully canceled. In this section, we provide a systematic understanding of how to evaluate the sensitivity for a given sensing sequence, which is determined by the difference between the largest and smallest eigenvalues of the transformed toggling frame operator; in addition, we provide simple examples to illustrate this. We leave the systematic design of sensing-oriented pulse sequences for higher spin systems to future work.

In order to perform quantum sensing, we add to the Hamiltonian a term corresponding to the target sensing field:

$$H = H_{\mathrm{dis}} + H_{\mathrm{int}} + H_{\mathrm{sense}}. \tag{14}$$

We focus on the case of sensing time-dependent magnetic fields, where $H_{\mathrm{sense}}(t) = \sum_i B(t) S_i^z$, although the same techniques can be readily adapted to electric field or strain sensing, among others. Note that the rotating wave approximation implies that H_{sense} will be diagonal, regardless of the type of target sensing field, and can thus be written as a polynomial in S_i^z.

Under the Hamiltonian engineering transformations, the sensing Hamiltonian will be transformed accordingly, and the effective average Hamiltonian contribution becomes

$$\bar{H}_{\mathrm{sense}} = \frac{1}{T} \int_0^T dt B(t) \tilde{S}_i^z(t). \tag{15}$$

This can be readily evaluated based on the instantaneous toggling frame transformations $\tilde{S}^z(t)$.

The sensitivity to an external magnetic field is generally characterized by the quantum Fisher information (QFI) [3,89]. In our case, since the sensing field only involves single-body operators, we can directly read off the optimal initial state and measurement axis that maximizes the QFI; we simply prepare an equal superposition between the eigenstates of $\bar{H}_{\mathrm{sense}}$ with the largest and smallest eigenvalues, and perform a Ramsey experiment within this two-level subspace. This method maximizes the amount of phase accumulation under a weak perturbation, achieving the best possible magnetic field sensitivity for a given pulse sequence.

Let us illustrate this case with a few concrete examples. First, consider the case of quantum sensing with interacting spin-$\frac{1}{2}$ ensembles. As described in Refs. [20,75], the conditions for interaction decoupling transform the original target sensing field BS^z into an effective sensing field

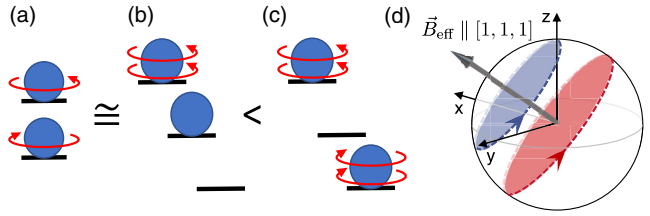

FIG. 11. Sensing with higher spin. (a) Sensing with spin-$\frac{1}{2}$ particles involves preparing spins in an equal superposition of the two basis states. Preparing the same initial state in a spin-1 system (b) yields a worse sensitivity than preparing a superposition of maximal and minimal eigenvalues in the spin-1 system (c). The number of arrows in (a–c) represents the phase accumulation speed. (d) Preparing the initial state to be an equal superposition of the largest and smallest eigenvalues maximizes precession. For the spin-$\frac{1}{2}$ case, this result is achieved by preparing an initial state that is perpendicular to the effective field, as shown by the red circle.

$B(S^x + S^y + S^z)/\sqrt{3}$. The largest and smallest eigenvectors are spin states aligned and anti-aligned with the sensing field direction, and the optimal initial state will be a spin state prepared in the plane orthogonal to the sensing field. Thus, the precession around the sensing field is maximized, as illustrated in Fig. 11(d), consistent with the results of Ref. [75].

We can also use the same technique to calculate the sensitivity of existing pulse sequences in the literature to a dc magnetic field. For simplicity, we assume ideal, infinitely fast pulses and consider the average Hamiltonian contribution from a dc magnetic field for both spin-1 pulse sequences considered in Refs. [22,54], as well as the famous spin-$\frac{1}{2}$ WAHUHA sequence in Ref. [20]. The average Hamiltonian $\bar{H}_{\text{sense}}$ and its eigenvalues λ are summarized in Table I, where we see a larger eigenvalue difference $\Delta\lambda$ for the two spin-1 sequences compared to the spin-$\frac{1}{2}$ sequence, indicating a higher-spin-enhanced sensitivity. We also find that, contrary to the suggestion in Ref. [54] that HoRD-qutrit-8 is better for sensing, the sequence CYL-6 in Ref. [22] has a larger eigenvalue difference, implying a higher sensitivity when preparing the optimal initial state. This finding highlights the importance of evaluating sensitivity using our approach of examining eigenvalue differences.

TABLE I. $\bar{H}_{\text{sense}}$ and λ for three sensing sequences. We see a larger $\Delta\lambda$ for the two spin-1 sequences compared to the spin-$\frac{1}{2}$ sequence, indicating a higher-spin-enhanced sensitivity. By further comparing the two spin-1 sequences, we see that their eigenvalue differences $\Delta\lambda$ are not the same, and CYL-6 has a larger eigenvalue difference despite having smaller diagonal matrix elements.

Sequence name	$\bar{H}_{\text{sense}}$	λ	$\Delta\lambda$
WAHUHA [20]	$\begin{pmatrix} \frac{1}{6} & \frac{1-i}{6} \\ \frac{1+i}{6} & -\frac{1}{6} \end{pmatrix}$	-0.289 0.289	0.577
CYL-6 [22]	$\begin{pmatrix} \frac{1}{6} & \frac{\sqrt{2}i}{6} & -\frac{i}{6} \\ -\frac{\sqrt{2}i}{6} & 0 & -\frac{\sqrt{2}}{6} \\ \frac{i}{6} & -\frac{\sqrt{2}}{6} & -\frac{1}{6} \end{pmatrix}$	-0.333 -0.122 0.455	0.789
HoRD-qutrit-8 [54]	$\begin{pmatrix} \frac{1}{3} & 0 & 0 \\ 0 & 0 & 0 \\ 0 & 0 & -\frac{1}{3} \end{pmatrix}$	-0.333 0 0.333	0.667

The two example sequences (CYL-6 and HoRD-qutrit-8) are likely not optimal sensing sequences, but the physical picture we discussed here provides a convenient method to incorporate quantum sensing into the sequence design procedure. We can follow the same procedure as described in the preceding sections but add in maximizing metrological sensitivity as an additional design criteria in choosing the ordering of toggling frames. We leave the detailed design of such sequences to future work.

VIII. CONCLUSIONS

In this work, we introduced a graph-based framework for the design of robust Hamiltonian engineering sequences in qudit systems and used this to experimentally demonstrate the first full decoupling of qudit interactions. In particular, our experiments demonstrate that our robust qutrit disorder and interaction decoupling sequence DROID-C3PO results in a tenfold improvement in coherence time over existing sequences, highlighting the power of our design framework. This framework only requires tracking the transformation of the S^z operator under pulses (i.e., frames), significantly reducing the sequence search space compared to prior approaches. Furthermore, by keeping track of all experimentally implementable connections between frames, we reduced the sequence construction into a simple graph traversal problem, avoiding the complicated, unstructured algebraic simplifications in prior approaches. Finally, we showed how pulses that transform S^z along geodesics lead to the natural and elegant incorporation of robustness considerations into our framework.

Our work also opens up new opportunities for future studies. For quantum many-body physics, higher spins enable new classes of Hamiltonians and phenomena, including quantum many-body scars [32–34], new spin-exchange channels [36,37], lattice gauge theories [16,90–97], and $SU(N)$ magnetism [50,51]. With larger Hilbert space dimensions, it also becomes possible to detect the Berry phase on a subsystem by using the additional levels as a phase reference. This opportunity may enable the study of interesting topological phenomena in Floquet engineered systems [98]. In quantum metrology, the larger spin translates to a larger dipole moment for enhanced sensing [38–40], and in our experimental platform of interacting NV ensembles, using the full spin-1 degree of freedom allows time-reversal operations that are not readily accessible with two levels [22], which are crucial for

entanglement-enhanced metrology [41,42] and measurements of out-of-time-ordered correlators (OTOCs) [99]. In quantum computation, where the use of qudits may have some advantages over qubits in gate complexity [100–103], our decoupling sequence can be applied to preserve quantum information for longer timescales [104] and allow for more quantum operations within the coherence time. Finally, as a generic framework, our method can be used to design practical decoupling or Hamiltonian engineering sequences for a wide range of experimental platforms, even if they have different dominant decoherence channels or spin greater than 1. These results may have wide-ranging implications for a number of different experimental systems beyond NV centers, including quadrupolar NMR [44–46], cold molecules [47,48], and nuclear spins or hyperfine states in trapped atoms [49–53].

ACKNOWLEDGMENTS

We thank J. Choi, S. Choi, C. Hart, W. W. Ho, N. Maskara, J. T. Oon, H. Pichler, C. Ramanathan, and Q.-Z. Zhu for helpful discussions. This work was supported in part by the Center for Ultracold Atoms (an NSF Physics Frontiers Center), NSSEFF (National Security Science and Engineering Faculty Fellowship), Gordon and Betty Moore Foundation Grant No. 7797-01, DARPA DRINQS (Defense Advanced Research Projects Agency, Driven and Non-equilibrium Quantum Systems Program), and National Science Foundation Grant No. PHY-2012023.

APPENDIX A: DEFINITIONS AND PROOFS

1. Convention for Gell-Mann matrices

For qutrit Hamiltonians, we adopt the following convention for the Gell-Mann basis, where the basis elements are defined as

$$\lambda_1 = \begin{pmatrix} 0 & 1 & 0 \\ 1 & 0 & 0 \\ 0 & 0 & 0 \end{pmatrix}, \quad \lambda_2 = \begin{pmatrix} 0 & -i & 0 \\ i & 0 & 0 \\ 0 & 0 & 0 \end{pmatrix}, \quad \lambda_3 = \begin{pmatrix} 1 & 0 & 0 \\ 0 & -1 & 0 \\ 0 & 0 & 0 \end{pmatrix}, \quad \lambda_4 = \begin{pmatrix} 0 & 0 & 1 \\ 0 & 0 & 0 \\ 1 & 0 & 0 \end{pmatrix},$$
$$\lambda_5 = \begin{pmatrix} 0 & 0 & -i \\ 0 & 0 & 0 \\ i & 0 & 0 \end{pmatrix}, \quad \lambda_6 = \begin{pmatrix} 0 & 0 & 0 \\ 0 & 0 & 1 \\ 0 & 1 & 0 \end{pmatrix}, \quad \lambda_7 = \begin{pmatrix} 0 & 0 & 0 \\ 0 & 0 & -i \\ 0 & i & 0 \end{pmatrix}, \quad \lambda_8 = \frac{1}{\sqrt{3}} \begin{pmatrix} 1 & 0 & 0 \\ 0 & 1 & 0 \\ 0 & 0 & -2 \end{pmatrix},$$
$$\lambda_0 = \sqrt{\frac{2}{3}} \begin{pmatrix} 1 & 0 & 0 \\ 0 & 1 & 0 \\ 0 & 0 & 1 \end{pmatrix}. \tag{A1}$$

2. Constraints on frame matrices

Generically, we can decompose the transformed $\tilde{S}^z$ operator in the generalized Gell-Mann basis $\{\lambda_\mu\}$ as $\tilde{S}^z_k = U^\dagger_{k-1} S^z U_{k-1} = \sum_\mu F_{\mu,k} \lambda_\mu$.

The frame matrices $F_{\mu,k}$ are required to satisfy certain constraints due to the frame transformation $U^\dagger S^z U$ being unitary. For example, for qubit systems, we require

$$F^2_{x,k} + F^2_{y,k} + F^2_{z,k} = 1 \tag{A2}$$

for all k.

For qudit systems, the constraint is that a unitary conjugation leaves the eigenvalues unchanged, such that $U^\dagger_{k-1} S^z U_{k-1} = \sum_\mu F_{\mu,k} \lambda_\mu$ should have the same set of eigenvalues as S^z. As an example, for qutrit systems, the following requirements are imposed,

$$F_1^2 + F_2^2 + F_3^2 + F_4^2 + F_5^2 + F_6^2 + F_7^2 + F_8^2 = 1, \tag{A3}$$

$$\frac{2F_8^3}{3\sqrt{3}} - \frac{2F_1^2 F_8}{\sqrt{3}} - \frac{2F_2^2 F_8}{\sqrt{3}} - \frac{2F_3^2 F_8}{\sqrt{3}} + \frac{F_4^2 F_8}{\sqrt{3}} + \frac{F_5^2 F_8}{\sqrt{3}} + \frac{F_6^2 F_8}{\sqrt{3}} + \frac{F_7^2 F_8}{\sqrt{3}} - F_3 F_4^2 - F_3 F_5^2 + F_3 F_6^2 + F_3 F_7^2 - 2F_1 F_4 F_6 - 2F_2 F_5 F_6 + 2F_2 F_4 F_7 - 2F_1 F_5 F_7 = 0, \tag{A4}$$

where we have dropped the k index for simplicity.

3. Proof of Theorem III.1

We can rewrite the condition $U_1^\dagger S^z U_1 = U_2^\dagger S^z U_2$ as $[U_1 U_2^\dagger, S^z] = 0$, which implies that S^z and $U_1 U_2^\dagger$ are simultaneously diagonalizable. Since S^z has nondegenerate eigenvalues, this implies that the matrix $U_1 U_2^\dagger$ must also be diagonal. Moreover, the unitarity of U_1 and U_2 implies that $U_1 U_2^\dagger$ is also unitary. Combined, these imply that $U_1 U_2^\dagger$ is a composition of rotations around the $\hat{z}$ axis of individual transitions.

On the other hand, by definition, H is a qudit Hamiltonian satisfying the secular approximation on each transition; i.e., for any spin rotation U_z formed by the composition of rotations around the $\hat{z}$ axis of individual transitions, we have

$$(U_z^\dagger)^{\otimes n} H U_z^{\otimes n} = H. \tag{A5}$$

Since $U_1 U_2^\dagger$ belongs to the type of rotation U_z, we have

$$(U_2 U_1^\dagger)^{\otimes n} H (U_1 U_2^\dagger)^{\otimes n} = H, \tag{A6}$$

which implies

$$(U_1^\dagger)^{\otimes n} H U_1^{\otimes n} = (U_2^\dagger)^{\otimes n} H U_2^{\otimes n}. \tag{A7}$$

4. Proof of polynomial representation of Hamiltonian

In the case of spin-$\frac{1}{2}$ particles with two-body interactions, we have shown that the transformed Hamiltonian is a second-order polynomial in the coefficients of the Pauli decomposition of $U^\dagger S^z U$. In the more general case, we can generalize this idea as follows:

Theorem A.1. For a spin-$(d-1/2)$ (where d is the dimension of the local Hilbert space) secular Hamiltonian consisting of at most k-body terms, if the S^z operator is transformed as $U^\dagger S^z U = \sum_\mu a_\mu \lambda_\mu$, then the transformed Hamiltonian can be written as an order-$k(d-1)$ polynomial in a_μ.

Proof. First, we note that if the transformation of the S^z operator is specified, then so are the transformations of all powers of S^z since $U^\dagger (S^z)^m U = (U^\dagger S^z U)^m$. In addition, linear combinations of the zeroth to $(d-1)$th powers of the spin-$(d-1/2)$ operator S^z generate all diagonal matrices of dimension d. To generate off-diagonal matrices, we can make use of the spin-$(d-1/2)$ S^x operator and its powers: The product of diagonal matrices and S^x generates all matrices containing only elements on the 1-diagonal (i.e., the diagonal that is 1 element offset from the main diagonal), the product of diagonal matrices and $(S^x)^2$ generates all matrices containing only elements on the 2-diagonal, and so on.

Therefore, if we write the transformed spin operators as $\tilde{S}^z = U^\dagger S^z U = \sum_\mu a_\mu \lambda_\mu$ and $\tilde{S}^x = U^\dagger S^x U = \sum_\mu b_\mu \lambda_\mu$, then any other spin operator can be expressed as $\sum_\alpha f_\alpha(a_\mu, b_\mu)\lambda_\alpha$, with $f_\alpha(a_\mu, b_\mu)$ being a multivariate polynomial in a_μ, b_μ that is at most order $(d-1)$ in each a_μ. The Hamiltonian, consisting of at most k-body terms, can in turn be written as a polynomial,

$$\tilde{H} = \sum_{\alpha_1 \cdots \alpha_k} g_{\alpha_1 \cdots \alpha_k}(a_\mu, b_\mu) \lambda_{\alpha_1} \otimes \cdots \otimes \lambda_{\alpha_k}, \tag{A8}$$

where $g_{\alpha_1 \cdots \alpha_k}(a_\mu, b_\mu)$ is a multivariate polynomial in a_μ, b_μ that is at most order $k(d-1)$ in each a_μ.

At this point, our expression of the Hamiltonian still depends on both a_μ and b_μ. However, based on Theorem 3.1, we know that this can be simplified into a form that only contains a_μ. The constraints that can be used to perform this simplification are the preservation of eigenvalues (and thus the characteristic polynomial) under unitary transformations, e.g., $|\lambda I - \sum_\mu a_\mu \lambda_\mu| = |\lambda I - S^z|$. This result will give rise to polynomial constraint equations within a_μ values as well as between a_μ and b_μ. Crucially, the imposition of these equations to simplify $g_{\alpha_1 \cdots \alpha_k}(a_\mu, b_\mu)$ can only lead to a reduction of the order of the polynomial in a_μ. Therefore, we see that the final expression for the Hamiltonian in terms of a_μ will be a polynomial of order at most $k(d-1)$. ∎

Explicit expressions for the polynomial can be elegantly obtained using representation theory of Lie groups, as described in more detail in an accompanying paper, Ref. [72]. For completeness, the explicit expression for the qutrit dipolar interaction is documented in Appendix A 6.

5. Proof of Theorem III.2

According to Appendix A 3, two unitaries U_1 and U_2 leading to the same frame $\tilde{S}^z = U_1^\dagger S^z U_1 = U_2^\dagger S^z U_2$ must satisfy $U_1 = U_{\text{phase}} U_2$. Plugging this requirement into the expression of $\tilde{S}^z_{\text{new}}$, we obtain

$$\begin{aligned}
\tilde{S}^z_{\text{new}} &= U_1^\dagger U_P^\dagger S^z U_P U_1 \\
&= U_2^\dagger U_{\text{phase}}^\dagger U_P^\dagger S^z U_P U_{\text{phase}} U_2 \\
&= U_2^\dagger (U_{\text{phase}}^\dagger U_P^\dagger U_{\text{phase}})(U_{\text{phase}}^\dagger S^z U_{\text{phase}}) \\
&\quad \times (U_{\text{phase}}^\dagger U_P U_{\text{phase}}) U_2 \\
&= U_2^\dagger (U_{\text{phase}}^\dagger U_P^\dagger U_{\text{phase}}) S^z (U_{\text{phase}}^\dagger U_P U_{\text{phase}}) U_2 \\
&= U_2^\dagger U_{P'}^\dagger S^z U_{P'} U_2,
\end{aligned} \tag{A9}$$

where $U_{P'} = U_{\text{phase}}^\dagger U_P U_{\text{phase}}$ is the phase conjugation of the original pulse U_P.

Since the pulse unitaries U_P and $U_{P'}$ are related by a phase conjugation, the underlying Hamiltonians that realize these unitaries are also related by the same phase conjugation. The effect of phase conjugation on a Hamiltonian is simply changing the phases of off-diagonal elements. As a concrete example, for a spin-1 system, a generic rotation generator matrix is transformed by a phase operator $U_{\text{phase}} = \text{diag}\{e^{i\theta_1}, e^{-i\theta_1 - i\theta_2}, e^{i\theta_2}\}$ as

$$\begin{aligned}
&U_{\text{phase}}^\dagger \begin{pmatrix} a_{11} & a_{12} & a_{13} \\ a_{21} & a_{22} & a_{23} \\ a_{31} & a_{32} & a_{33} \end{pmatrix} U_{\text{phase}} \\
&= \begin{pmatrix} a_{11} & a_{12} e^{-i(2\theta_1+\theta_2)} & a_{13} e^{i(\theta_2-\theta_1)} \\ a_{21} e^{i(2\theta_1+\theta_2)} & a_{22} & a_{23} e^{i(\theta_1+2\theta_2)} \\ a_{31} e^{i(\theta_1-\theta_2)} & a_{32} e^{-i(\theta_1+2\theta_2)} & a_{33} \end{pmatrix}.
\end{aligned} \tag{A10}$$

As one can see, the only effect is to change the phases of the drives applied on each transition, which does not change the experimental implementability of the pulses because selection rules are not concerned with phases.

6. Explicit expression for transformed qutrit dipolar Hamiltonian

The qutrit dipolar Hamiltonian [Eq. (9)] can be transformed to $\sum_{ij} a_{ij}\lambda_i \otimes \lambda_j$, where λ_i is the Gell-Mann basis (see Appendix A 1) and a_{ij} are coefficients that can be written as a fourth-order polynomial of the frame representation $\tilde{S}^z = \sum_i a_i\lambda_i$ according to Appendix A 4. The explicit expressions for a_{ij} are

$$
\begin{aligned}
a_{11} &= \frac{4a_8^4}{3} + \frac{4}{3}a_2^2a_8^2 + \frac{4}{3}a_3^2a_8^2 + \frac{4}{3}a_4^2a_8^2 + \frac{4}{3}a_5^2a_8^2 + \frac{4}{3}a_6^2a_8^2 + \frac{4}{3}a_7^2a_8^2 - \frac{4a_1a_4a_6a_8}{\sqrt{3}} - \frac{4a_1a_5a_7a_8}{\sqrt{3}} \\
&\quad + a_2^2 + a_3^2 + \frac{5a_4^2}{4} + \frac{5a_5^2}{4} - a_4^2a_6^2 + \frac{5a_6^2}{4} - a_5^2a_7^2 + \frac{5a_7^2}{4} - 2a_4a_5a_6a_7 - 1, \\
a_{12} &= a_6a_7a_4^2 - a_5a_6^2a_4 + a_5a_7^2a_4 - \frac{2a_2a_6a_8a_4}{\sqrt{3}} + \frac{2a_1a_7a_8a_4}{\sqrt{3}} - \frac{4}{3}a_1a_2a_8^2 - a_1a_2 - a_5^2a_6a_7 - \frac{2a_1a_5a_6a_8}{\sqrt{3}} - \frac{2a_2a_5a_7a_8}{\sqrt{3}}, \\
a_{13} &= -\frac{1}{2}a_6a_4^3 - \frac{1}{2}a_5a_7a_4^2 - \frac{a_1a_8a_4^2}{\sqrt{3}} + \frac{1}{2}a_6^3a_4 + \frac{1}{2}a_6a_7^2a_4 - \frac{1}{2}a_5^2a_6a_4 - \frac{2a_3a_6a_8a_4}{\sqrt{3}} + \frac{1}{2}a_5a_7^3 \\
&\quad - \frac{4}{3}a_1a_3a_8^2 - a_1a_3 - \frac{1}{2}a_5^3a_7 + \frac{1}{2}a_5a_6^2a_7 - \frac{a_1a_5^2a_8}{\sqrt{3}} + \frac{a_1a_6^2a_8}{\sqrt{3}} + \frac{a_1a_7^2a_8}{\sqrt{3}} - \frac{2a_3a_5a_7a_8}{\sqrt{3}}, \\
a_{14} &= -a_3a_6^3 - \frac{a_8a_6^3}{\sqrt{3}} + a_1a_4a_6^2 + 2a_2a_5a_6^2 - \frac{2a_8^3a_6}{3\sqrt{3}} + a_3a_5^2a_6 - a_3a_7^2a_6 + \frac{a_3a_6}{4} - a_2a_4a_7a_6 + a_1a_5a_7a_6 + \frac{2a_2^2a_8a_6}{\sqrt{3}} \\
&\quad + \frac{2a_3^2a_8a_6}{\sqrt{3}} - \frac{a_5^2a_8a_6}{\sqrt{3}} - \frac{a_7^2a_8a_6}{\sqrt{3}} + \frac{a_8a_6}{4\sqrt{3}} + a_2a_5a_7^2 + \frac{2}{3}a_1a_4a_8^2 - \frac{5a_1a_4}{4} - \frac{a_2a_5}{4} - a_3a_4a_5a_7 - \frac{2a_1a_3a_4a_8}{\sqrt{3}} \\
&\quad + \frac{2a_1a_2a_7a_8}{\sqrt{3}} + \frac{a_4a_5a_7a_8}{\sqrt{3}}, \\
a_{15} &= \frac{2a_8a_7^3}{\sqrt{3}} - a_1a_5a_7^2 + \frac{2a_8^3a_7}{\sqrt{3}} - a_3a_5^2a_7 + \frac{a_3a_7}{4} - a_1a_4a_6a_7 - a_2a_5a_6a_7 + \frac{2a_2^2a_8a_7}{\sqrt{3}} + \frac{2a_3^2a_8a_7}{\sqrt{3}} + \frac{2a_4^2a_8a_7}{\sqrt{3}} + \sqrt{3}a_5^2a_8a_7 \\
&\quad + \frac{2a_6^2a_8a_7}{\sqrt{3}} - \frac{7a_8a_7}{4\sqrt{3}} - a_2a_4a_6^2 + \frac{2}{3}a_1a_5a_8^2 + \frac{a_2a_4}{4} - \frac{5a_1a_5}{4} - a_3a_4a_5a_6 - \frac{2a_1a_3a_5a_8}{\sqrt{3}} - \frac{2a_1a_2a_6a_8}{\sqrt{3}} + \frac{a_4a_5a_6a_8}{\sqrt{3}}, \\
a_{16} &= \frac{2a_8a_4^3}{\sqrt{3}} - a_1a_6a_4^2 + \frac{2a_8^3a_4}{\sqrt{3}} + a_3a_6^2a_4 - \frac{a_3a_4}{4} - a_2a_5a_6a_4 - a_1a_5a_7a_4 + \frac{2a_2^2a_8a_4}{\sqrt{3}} + \frac{2a_3^2a_8a_4}{\sqrt{3}} + \frac{2a_5^2a_8a_4}{\sqrt{3}} + \sqrt{3}a_6^2a_8a_4 \\
&\quad + \frac{2a_7^2a_8a_4}{\sqrt{3}} - \frac{7a_8a_4}{4\sqrt{3}} + \frac{2}{3}a_1a_6a_8^2 - \frac{5a_1a_6}{4} - a_2a_5^2a_7 + \frac{a_2a_7}{4} + a_3a_5a_6a_7 - \frac{2a_1a_2a_5a_8}{\sqrt{3}} + \frac{2a_1a_3a_6a_8}{\sqrt{3}} + \frac{a_5a_6a_7a_8}{\sqrt{3}}, \\
a_{17} &= \frac{2a_8a_5^3}{\sqrt{3}} - a_1a_7a_5^2 + \frac{2a_8^3a_5}{\sqrt{3}} + a_3a_7^2a_5 - \frac{a_3a_5}{4} - a_1a_4a_6a_5 + a_2a_4a_7a_5 + \frac{2a_2^2a_8a_5}{\sqrt{3}} + \frac{2a_3^2a_8a_5}{\sqrt{3}} + \frac{2a_4^2a_8a_5}{\sqrt{3}} + \frac{2a_6^2a_8a_5}{\sqrt{3}} \\
&\quad + \sqrt{3}a_7^2a_8a_5 - \frac{7a_8a_5}{4\sqrt{3}} + \frac{2}{3}a_1a_7a_8^2 + a_2a_4^2a_6 - \frac{a_2a_6}{4} - \frac{5a_1a_7}{4} + a_3a_4a_6a_7 + \frac{2a_1a_2a_4a_8}{\sqrt{3}} + \frac{2a_1a_3a_7a_8}{\sqrt{3}} + \frac{a_4a_6a_7a_8}{\sqrt{3}}, \\
a_{18} &= \frac{1}{2}\sqrt{3}a_6a_4^3 + \frac{1}{2}\sqrt{3}a_5a_7a_4^2 + a_1a_8a_4^2 + \frac{1}{2}\sqrt{3}a_6^3a_4 + \frac{1}{2}\sqrt{3}a_6a_7^2a_4 + \frac{2a_6a_8^2a_4}{\sqrt{3}} + \frac{1}{2}\sqrt{3}a_5^2a_6a_4 - \frac{1}{2}\sqrt{3}a_6a_4 + \frac{1}{2}\sqrt{3}a_5a_7^3 \\
&\quad + \frac{4}{3}a_1a_8^3 + \frac{2a_5a_7a_8^2}{\sqrt{3}} + \frac{1}{2}\sqrt{3}a_5^3a_7 + \frac{1}{2}\sqrt{3}a_5a_6^2a_7 - \frac{1}{2}\sqrt{3}a_5a_7 + a_1a_5^2a_8 + a_1a_6^2a_8 + a_1a_7^2a_8 - 2a_1a_8, \\
a_{22} &= -\frac{4}{3}a_8^2a_2^2 - a_2^2 - \frac{4a_5a_6a_8a_2}{\sqrt{3}} + \frac{4a_4a_7a_8a_2}{\sqrt{3}} + \frac{a_4^2}{4} + \frac{a_5^2}{4} - a_5^2a_6^2 + \frac{a_6^2}{4} - a_4^2a_7^2 + \frac{a_7^2}{4} + \frac{a_8^2}{3} + 2a_4a_5a_6a_7,
\end{aligned}
$$

$$
\begin{aligned}
a_{23} &= \frac{1}{2}a_7a_4^3 - \frac{1}{2}a_5a_6a_4^2 - \frac{a_2a_8a_4^2}{\sqrt{3}} - \frac{1}{2}a_7^3a_4 + \frac{1}{2}a_5^2a_7a_4 - \frac{1}{2}a_6^2a_7a_4 + \frac{2a_3a_7a_8a_4}{\sqrt{3}} + \frac{1}{2}a_5a_6^3 \\
&\quad + \frac{1}{2}a_5a_6a_7^2 - \frac{4}{3}a_2a_3a_8^2 - a_2a_3 - \frac{1}{2}a_5^3a_6 - \frac{a_2a_5^2a_8}{\sqrt{3}} + \frac{a_2a_6^2a_8}{\sqrt{3}} + \frac{a_2a_7^2a_8}{\sqrt{3}} - \frac{2a_3a_5a_6a_8}{\sqrt{3}}, \\
a_{24} &= a_3a_7^3 + \sqrt{3}a_8a_7^3 + a_2a_4a_7^2 - 2a_1a_5a_7^2 + \frac{8a_8^3a_7}{3\sqrt{3}} - a_3a_5^2a_7 + a_3a_6^2a_7 - \frac{a_3a_7}{4} - a_1a_4a_6a_7 \\
&\quad - a_2a_5a_6a_7 + \frac{2a_2^2a_8a_7}{\sqrt{3}} + \frac{2a_4^2a_8a_7}{\sqrt{3}} + \sqrt{3}a_5^2a_8a_7 + \sqrt{3}a_6^2a_8a_7 - \frac{3}{4}\sqrt{3}a_8a_7 - a_1a_5a_6^2 \\
&\quad + \frac{2}{3}a_2a_4a_8^2 - \frac{5a_2a_4}{4} + \frac{a_1a_5}{4} - a_3a_4a_5a_6 - \frac{2a_2a_3a_4a_8}{\sqrt{3}} - \frac{2a_1a_2a_6a_8}{\sqrt{3}} + \frac{a_4a_5a_6a_8}{\sqrt{3}}, \\
a_{25} &= -\frac{2a_6a_8a_2^2}{\sqrt{3}} - a_5a_6^2a_2 + \frac{2}{3}a_5a_8^2a_2 - \frac{5a_5a_2}{4} + a_4a_6a_7a_2 - \frac{2a_3a_5a_8a_2}{\sqrt{3}} - \frac{2a_1a_7a_8a_2}{\sqrt{3}} + a_1a_4a_7^2 \\
&\quad - \frac{a_1a_4}{4} - a_3a_5^2a_6 + \frac{a_3a_6}{4} + a_3a_4a_5a_7 - a_1a_5a_6a_7 + \frac{a_5^2a_6a_8}{\sqrt{3}} + \frac{a_6a_8}{4\sqrt{3}} - \frac{a_4a_5a_7a_8}{\sqrt{3}}, \\
a_{26} &= -\frac{2a_5a_8a_2^2}{\sqrt{3}} + \frac{2}{3}a_6a_8^2a_2 - a_5^2a_6a_2 - \frac{5a_6a_2}{4} + a_4a_5a_7a_2 - \frac{2a_1a_4a_8a_2}{\sqrt{3}} + \frac{2a_3a_6a_8a_2}{\sqrt{3}} + a_3a_5a_6^2 \\
&\quad - \frac{a_3a_5}{4} - a_1a_4a_5a_6 + a_1a_4^2a_7 - \frac{a_1a_7}{4} - a_3a_4a_6a_7 + \frac{a_5a_6^2a_8}{\sqrt{3}} + \frac{a_5a_8}{4\sqrt{3}} - \frac{a_4a_6a_7a_8}{\sqrt{3}}, \\
a_{27} &= \frac{2a_4a_8a_2^2}{\sqrt{3}} + \frac{2}{3}a_7a_8^2a_2 + a_4a_5a_6a_2 - a_4^2a_7a_2 - \frac{5a_7a_2}{4} - \frac{2a_1a_5a_8a_2}{\sqrt{3}} + \frac{2a_3a_7a_8a_2}{\sqrt{3}} - a_3a_4a_7^2 \\
&\quad + \frac{a_3a_4}{4} - a_1a_5^2a_6 + \frac{a_1a_6}{4} + a_1a_4a_5a_7 + a_3a_5a_6a_7 - \frac{a_4a_7^2a_8}{\sqrt{3}} - \frac{a_4a_8}{4\sqrt{3}} + \frac{a_5a_6a_7a_8}{\sqrt{3}}, \\
a_{28} &= -\frac{1}{2}\sqrt{3}a_7a_4^3 + \frac{1}{2}\sqrt{3}a_5a_6a_4^2 + a_2a_8a_4^2 - \frac{1}{2}\sqrt{3}a_7^3a_4 - \frac{2a_7a_8^2a_4}{\sqrt{3}} - \frac{1}{2}\sqrt{3}a_5^2a_7a_4 - \frac{1}{2}\sqrt{3}a_6^2a_7a_4 + \frac{1}{2}\sqrt{3}a_7a_4 + \frac{1}{2}\sqrt{3}a_5a_6^3 \\
&\quad + \frac{4}{3}a_2a_8^3 + \frac{1}{2}\sqrt{3}a_5a_6a_7^2 + \frac{2a_5a_6a_8^2}{\sqrt{3}} + \frac{1}{2}\sqrt{3}a_5^3a_6 - \frac{1}{2}\sqrt{3}a_5a_6 + a_2a_5^2a_8 + a_2a_6^2a_8 + a_2a_7^2a_8 - 2a_2a_8, \\
a_{33} &= -\frac{a_4^4}{4} - \frac{1}{2}a_5^2a_4^2 + \frac{1}{2}a_6^2a_4^2 + \frac{1}{2}a_7^2a_4^2 - 2a_8^2a_4^2 + \frac{a_4^2}{4} + \frac{4a_1a_6a_8a_4}{\sqrt{3}} - \frac{4a_2a_7a_8a_4}{\sqrt{3}} - \frac{a_5^4}{4} - \frac{a_6^4}{4} - \frac{a_7^4}{4} - \frac{16a_8^4}{9} - a_3^2 + \frac{a_5^2}{4} \\
&\quad + \frac{1}{2}a_5^2a_6^2 + \frac{a_6^2}{4} + \frac{1}{2}a_5^2a_7^2 - \frac{1}{2}a_6^2a_7^2 + \frac{a_7^2}{4} - \frac{4}{3}a_3^2a_8^2 - 2a_5^2a_8^2 - 2a_6^2a_8^2 - 2a_7^2a_8^2 + \frac{5a_8^2}{3} + \frac{4a_2a_5a_6a_8}{\sqrt{3}} + \frac{4a_1a_5a_7a_8}{\sqrt{3}}, \\
a_{34} &= -\frac{a_8a_4^3}{\sqrt{3}} + \frac{1}{2}a_1a_6a_4^2 - \frac{1}{2}a_2a_7a_4^2 - \frac{4a_8^3a_4}{3\sqrt{3}} + \frac{2}{3}a_3a_8^2a_4 - \frac{5a_3a_4}{4} + a_2a_5a_6a_4 + a_1a_5a_7a_4 \\
&\quad - \frac{2a_3^2a_8a_4}{\sqrt{3}} - \frac{a_5^2a_8a_4}{\sqrt{3}} - \frac{2a_6^2a_8a_4}{\sqrt{3}} - \frac{2a_7^2a_8a_4}{\sqrt{3}} + \frac{5a_8a_4}{4\sqrt{3}} + \frac{1}{2}a_1a_6^3 - \frac{1}{2}a_2a_7^3 + \frac{1}{2}a_1a_6a_7^2 \\
&\quad - \frac{1}{2}a_1a_5^2a_6 - \frac{a_1a_6}{4} + \frac{1}{2}a_2a_5^2a_7 - \frac{1}{2}a_2a_6^2a_7 + \frac{a_2a_7}{4} - \frac{2a_1a_3a_6a_8}{\sqrt{3}} + \frac{2a_2a_3a_7a_8}{\sqrt{3}}, \\
a_{35} &= -\frac{a_8a_5^3}{\sqrt{3}} + \frac{1}{2}a_2a_6a_5^2 + \frac{1}{2}a_1a_7a_5^2 - \frac{4a_8^3a_5}{3\sqrt{3}} + \frac{2}{3}a_3a_8^2a_5 - \frac{5a_3a_5}{4} + a_1a_4a_6a_5 - a_2a_4a_7a_5 \\
&\quad - \frac{2a_3^2a_8a_5}{\sqrt{3}} - \frac{a_4^2a_8a_5}{\sqrt{3}} - \frac{2a_6^2a_8a_5}{\sqrt{3}} - \frac{2a_7^2a_8a_5}{\sqrt{3}} + \frac{5a_8a_5}{4\sqrt{3}} + \frac{1}{2}a_2a_6^3 + \frac{1}{2}a_1a_7^3 + \frac{1}{2}a_2a_6a_7^2 \\
&\quad - \frac{1}{2}a_2a_4^2a_6 - \frac{a_2a_6}{4} - \frac{1}{2}a_1a_4^2a_7 + \frac{1}{2}a_1a_6^2a_7 - \frac{a_1a_7}{4} - \frac{2a_2a_3a_6a_8}{\sqrt{3}} - \frac{2a_1a_3a_7a_8}{\sqrt{3}},
\end{aligned}
$$

$$
\begin{aligned}
a_{36} &= -\frac{1}{2}a_1a_4^3 - \frac{1}{2}a_2a_5a_4^2 + \frac{2a_6a_8a_4^2}{\sqrt{3}} - \frac{1}{2}a_1a_5^2a_4 - \frac{1}{2}a_1a_6^2a_4 + \frac{1}{2}a_1a_7^2a_4 + \frac{a_1a_4}{4} + a_2a_6a_7a_4 \\
&\quad - \frac{2a_1a_3a_8a_4}{\sqrt{3}} - \frac{1}{2}a_2a_5^3 + \frac{4a_6a_8^3}{3\sqrt{3}} - \frac{1}{2}a_2a_5a_6^2 + \frac{1}{2}a_2a_5a_7^2 + \frac{2}{3}a_3a_6a_8^2 + \frac{a_2a_5}{4} - \frac{5a_3a_6}{4} \\
&\quad - a_1a_5a_6a_7 + \frac{a_6^3a_8}{\sqrt{3}} + \frac{a_6a_7^2a_8}{\sqrt{3}} - \frac{2a_2a_3a_5a_8}{\sqrt{3}} + \frac{2a_3^2a_6a_8}{\sqrt{3}} + \frac{2a_5^2a_6a_8}{\sqrt{3}} - \frac{5a_6a_8}{4\sqrt{3}}, \\
a_{37} &= \frac{1}{2}a_2a_4^3 - \frac{1}{2}a_1a_5a_4^2 + \frac{2a_7a_8a_4^2}{\sqrt{3}} + \frac{1}{2}a_2a_5^2a_4 - \frac{1}{2}a_2a_6^2a_4 + \frac{1}{2}a_2a_7^2a_4 - \frac{a_2a_4}{4} - a_1a_6a_7a_4 \\
&\quad + \frac{2a_2a_3a_8a_4}{\sqrt{3}} - \frac{1}{2}a_1a_5^3 + \frac{4a_7a_8^3}{3\sqrt{3}} + \frac{1}{2}a_1a_5a_6^2 - \frac{1}{2}a_1a_5a_7^2 + \frac{2}{3}a_3a_7a_8^2 + \frac{a_1a_5}{4} - \frac{5a_3a_7}{4} \\
&\quad - a_2a_5a_6a_7 + \frac{a_7^3a_8}{\sqrt{3}} - \frac{2a_1a_3a_5a_8}{\sqrt{3}} + \frac{2a_3^2a_7a_8}{\sqrt{3}} + \frac{2a_5^2a_7a_8}{\sqrt{3}} + \frac{a_6^2a_7a_8}{\sqrt{3}} - \frac{5a_7a_8}{4\sqrt{3}}, \\
a_{38} &= \frac{1}{4}\sqrt{3}a_4^4 + \frac{1}{2}\sqrt{3}a_5^2a_4^2 + \frac{4a_8^2a_4^2}{\sqrt{3}} - \frac{1}{4}\sqrt{3}a_4^2 - 2a_1a_6a_8a_4 + 2a_2a_7a_8a_4 + \frac{1}{4}\sqrt{3}a_5^4 - \frac{1}{4}\sqrt{3}a_6^4 \\
&\quad - \frac{1}{4}\sqrt{3}a_7^4 + \frac{8a_8^4}{3\sqrt{3}} + \frac{4}{3}a_3a_8^3 - \frac{1}{4}\sqrt{3}a_5^2 + \frac{1}{4}\sqrt{3}a_6^2 - \frac{1}{2}\sqrt{3}a_6^2a_7^2 + \frac{1}{4}\sqrt{3}a_7^2 + \frac{4a_5^2a_8^2}{\sqrt{3}} \\
&\quad + \frac{2a_6^2a_8^2}{\sqrt{3}} + \frac{2a_7^2a_8^2}{\sqrt{3}} - \frac{2a_8^2}{\sqrt{3}} + 2a_3a_6^2a_8 + 2a_3a_7^2a_8 - 2a_3a_8 - 2a_2a_5a_6a_8 - 2a_1a_5a_7a_8, \\
a_{44} &= a_6^4 + a_2^2a_6^2 + a_4^2a_6^2 + a_5^2a_6^2 + a_7^2a_6^2 - \frac{4a_3a_8a_6^2}{\sqrt{3}} - a_6^2 + 2a_2a_3a_5a_6 + 2a_1a_2a_7a_6 + \frac{4a_1a_4a_8a_6}{\sqrt{3}} \\
&\quad + \frac{2a_2a_5a_8a_6}{\sqrt{3}} - \frac{8a_8^4}{9} - \frac{8a_3a_8^3}{3\sqrt{3}} - \frac{5a_4^2}{4} + a_3^2a_5^2 - \frac{a_5^2}{4} - a_2^2a_7^2 - a_3^2a_7^2 - \frac{4}{3}a_4^2a_8^2 - a_5^2a_8^2 - a_7^2a_8^2 \\
&\quad + \frac{a_8^2}{2} + 2a_1a_3a_5a_7 - \frac{2a_3a_5^2a_8}{\sqrt{3}} - \frac{4a_3a_7^2a_8}{\sqrt{3}} + \frac{1}{2}\sqrt{3}a_3a_8 - \frac{4a_2a_4a_7a_8}{\sqrt{3}} + \frac{2a_1a_5a_7a_8}{\sqrt{3}} + \frac{1}{4}, \\
a_{45} &= a_7a_6^3 - a_1a_2a_6^2 + a_7^3a_6 + a_7a_8^2a_6 - a_2a_3a_4a_6 - a_1a_3a_5a_6 + 2a_2^2a_7a_6 + a_3^2a_7a_6 + a_4^2a_7a_6 + a_5^2a_7a_6 - a_7a_6 + \frac{a_2a_4a_8a_6}{\sqrt{3}} \\
&\quad + \frac{a_1a_5a_8a_6}{\sqrt{3}} + a_1a_2a_7^2 - \frac{1}{3}a_4a_5a_8^2 - a_3^2a_4a_5 - a_4a_5 - a_1a_3a_4a_7 + a_2a_3a_5a_7 + \frac{2a_3a_4a_5a_8}{\sqrt{3}} + \frac{a_1a_4a_7a_8}{\sqrt{3}} - \frac{a_2a_5a_7a_8}{\sqrt{3}}, \\
a_{46} &= -a_6a_4^3 - 2a_5a_7a_4^2 - \frac{2a_1a_8a_4^2}{\sqrt{3}} - a_6^3a_4 - a_6a_7^2a_4 - \frac{4}{3}a_6a_8^2a_4 - a_2a_3a_5a_4 - a_2^2a_6a_4 - a_5^2a_6a_4 - \frac{a_6a_4}{4} - a_1a_2a_7a_4 \\
&\quad + \frac{a_2a_5a_8a_4}{\sqrt{3}} - 2a_5a_7^3 - \frac{8a_1a_8^3}{3\sqrt{3}} + a_1a_3a_5^2 - a_1a_3a_7^2 - 2a_5a_7a_8^2 + a_1a_2a_5a_6 - 2a_5^3a_7 - 2a_5a_6^2a_7 - a_2^2a_5a_7 \\
&\quad - 2a_3^2a_5a_7 + \frac{7a_5a_7}{4} - a_2a_3a_6a_7 - \sqrt{3}a_1a_5^2a_8 - \frac{2a_1a_6^2a_8}{\sqrt{3}} - \sqrt{3}a_1a_7^2a_8 + \frac{1}{2}\sqrt{3}a_1a_8 - \frac{a_2a_6a_7a_8}{\sqrt{3}}, \\
a_{47} &= a_6a_5^3 - a_2a_3a_5^2 + \sqrt{3}a_2a_8a_5^2 + a_6^3a_5 + a_6a_7^2a_5 + a_6a_8^2a_5 - a_1a_3a_4a_5 - a_2^2a_6a_5 + a_3^2a_6a_5 + a_4^2a_6a_5 \\
&\quad - \frac{3a_6a_5}{4} - a_1a_2a_7a_5 + \frac{a_1a_4a_8a_5}{\sqrt{3}} + \frac{8a_2a_8^3}{3\sqrt{3}} + a_2a_3a_6^2 - \frac{1}{3}a_4a_7a_8^2 - a_1a_2a_4a_6 + a_2^2a_4a_7 + a_3^2a_4a_7 \\
&\quad - \frac{5a_4a_7}{4} + a_1a_3a_6a_7 + \frac{2a_2a_4^2a_8}{\sqrt{3}} + \sqrt{3}a_2a_6^2a_8 + \frac{2a_2a_7^2a_8}{\sqrt{3}} - \frac{1}{2}\sqrt{3}a_2a_8 + \frac{a_1a_6a_7a_8}{\sqrt{3}},
\end{aligned}
$$

$$a_{48} = a_8 a_4^3 - \frac{1}{2}\sqrt{3}a_1 a_6 a_4^2 + \frac{1}{2}\sqrt{3}a_2 a_7 a_4^2 + \frac{2}{3}a_8^3 a_4 + \sqrt{3}a_3 a_6^2 a_4 + \sqrt{3}a_3 a_7^2 a_4 + \frac{2a_3 a_8^2 a_4}{\sqrt{3}} - \frac{1}{4}\sqrt{3}a_3 a_4 - \sqrt{3}a_2 a_5 a_6 a_4$$
$$- \sqrt{3}a_1 a_5 a_7 a_4 + a_5^2 a_8 a_4 + a_6^2 a_8 a_4 + a_7^2 a_8 a_4 - \frac{7a_8 a_4}{4} + \frac{1}{2}\sqrt{3}a_1 a_6^3 - \frac{1}{2}\sqrt{3}a_2 a_7^3 + \frac{1}{2}\sqrt{3}a_1 a_6 a_7^2 + \frac{2a_1 a_6 a_8^2}{\sqrt{3}}$$
$$- \frac{2a_2 a_7 a_8^2}{\sqrt{3}} + \frac{1}{2}\sqrt{3}a_1 a_5^2 a_6 - \frac{1}{4}\sqrt{3}a_1 a_6 - \frac{1}{2}\sqrt{3}a_2 a_5^2 a_7 - \frac{1}{2}\sqrt{3}a_2 a_6^2 a_7 + \frac{1}{4}\sqrt{3}a_2 a_7,$$

$$a_{55} = a_7^4 + a_2^2 a_7^2 + a_3^2 a_7^2 + a_4^2 a_7^2 + a_5^2 a_7^2 + a_6^2 a_7^2 + a_8^2 a_7^2 - a_7^2 - 2a_1 a_3 a_5 a_7 - 2a_1 a_2 a_6 a_7 + \frac{2a_1 a_5 a_8 a_7}{\sqrt{3}} - \frac{a_4^2}{4}$$
$$- a_3^2 a_5^2 - \frac{5a_5^2}{4} - a_2^2 a_6^2 - \frac{1}{3}a_5^2 a_8^2 - \frac{a_8^2}{6} - 2a_2 a_3 a_5 a_6 + \frac{2a_3 a_5^2 a_8}{\sqrt{3}} - \frac{a_3 a_8}{2\sqrt{3}} + \frac{2a_2 a_5 a_6 a_8}{\sqrt{3}} + \frac{1}{4},$$

$$a_{56} = a_7 a_4^3 + a_7^3 a_4 + a_7 a_8^2 a_4 - a_1 a_3 a_5 a_4 - a_1 a_2 a_6 a_4 + a_2^2 a_7 a_4 + a_3^2 a_7 a_4 + a_5^2 a_7 a_4 + a_6^2 a_7 a_4 - \frac{3a_7 a_4}{4} + \frac{a_1 a_5 a_8 a_4}{\sqrt{3}} - a_2 a_3 a_5^2$$
$$+ a_2 a_3 a_6^2 - \frac{1}{3}a_5 a_6 a_8^2 - a_2^2 a_5 a_6 + a_3^2 a_5 a_6 - \frac{5a_5 a_6}{4} - a_1 a_2 a_5 a_7 + a_1 a_3 a_6 a_7 + \frac{a_2 a_5^2 a_8}{\sqrt{3}} + \frac{a_2 a_6^2 a_8}{\sqrt{3}} - \frac{a_2 a_8}{2\sqrt{3}} + \frac{a_1 a_6 a_7 a_8}{\sqrt{3}},$$

$$a_{57} = a_7 a_5^3 - a_1 a_3 a_5^2 + \frac{a_1 a_8 a_5^2}{\sqrt{3}} + a_7^3 a_5 + \frac{2}{3}a_7 a_8^2 a_5 + a_2 a_3 a_4 a_5 - a_1 a_2 a_6 a_5 + a_2^2 a_7 a_5 + 2a_3^2 a_7 a_5 + a_4^2 a_7 a_5 + a_6^2 a_7 a_5$$
$$- \frac{9a_7 a_5}{4} - \frac{a_2 a_4 a_8 a_5}{\sqrt{3}} + a_1 a_3 a_7^2 + a_2^2 a_4 a_6 - \frac{a_4 a_6}{4} + a_1 a_2 a_4 a_7 + a_2 a_3 a_6 a_7 + \frac{a_1 a_7^2 a_8}{\sqrt{3}} - \frac{a_1 a_8}{2\sqrt{3}} + \frac{a_2 a_6 a_7 a_8}{\sqrt{3}},$$

$$a_{58} = a_8 a_5^3 - \frac{1}{2}\sqrt{3}a_2 a_6 a_5^2 - \frac{1}{2}\sqrt{3}a_1 a_7 a_5^2 + \frac{2}{3}a_8^3 a_5 + \sqrt{3}a_3 a_6^2 a_5 + \sqrt{3}a_3 a_7^2 a_5 + \frac{2a_3 a_8^2 a_5}{\sqrt{3}} - \frac{1}{4}\sqrt{3}a_3 a_5 - \sqrt{3}a_1 a_4 a_6 a_5$$
$$+ \sqrt{3}a_2 a_4 a_7 a_5 + a_4^2 a_8 a_5 + a_6^2 a_8 a_5 + a_7^2 a_8 a_5 - \frac{7a_8 a_5}{4} + \frac{1}{2}\sqrt{3}a_2 a_6^3 + \frac{1}{2}\sqrt{3}a_1 a_7^3 + \frac{1}{2}\sqrt{3}a_2 a_6 a_7^2 + \frac{2a_2 a_6 a_8^2}{\sqrt{3}}$$
$$+ \frac{2a_1 a_7 a_8^2}{\sqrt{3}} + \frac{1}{2}\sqrt{3}a_2 a_4^2 a_6 - \frac{1}{4}\sqrt{3}a_2 a_6 + \frac{1}{2}\sqrt{3}a_1 a_4^2 a_7 + \frac{1}{2}\sqrt{3}a_1 a_6^2 a_7 - \frac{1}{4}\sqrt{3}a_1 a_7,$$

$$a_{66} = a_4^4 + a_2^2 a_4^2 + a_5^2 a_4^2 + a_6^2 a_4^2 + a_7^2 a_4^2 + 4a_8^2 a_4^2 - a_4^2 - 2a_1 a_2 a_5 a_4 + 2a_2 a_3 a_7 a_4 - \frac{4a_1 a_6 a_8 a_4}{\sqrt{3}} + 2\sqrt{3}a_2 a_7 a_8 a_4$$
$$+ \frac{8a_8^4}{3} + \frac{8a_3 a_8^3}{3\sqrt{3}} - a_2^2 a_5^2 - a_3^2 a_5^2 - \frac{5a_6^2}{4} + a_3^2 a_7^2 - \frac{a_7^2}{4} + 3a_5^2 a_8^2 + \frac{8}{3}a_6^2 a_8^2 + 3a_7^2 a_8^2 - \frac{13a_8^2}{6}$$
$$- 2a_1 a_3 a_5 a_7 + \frac{4a_3 a_6^2 a_8}{\sqrt{3}} + 2\sqrt{3}a_3 a_7^2 a_8 - \frac{1}{2}\sqrt{3}a_3 a_8 - \frac{4a_2 a_5 a_6 a_8}{\sqrt{3}} - 2\sqrt{3}a_1 a_5 a_7 a_8 + \frac{1}{4},$$

$$a_{67} = a_5 a_4^3 + a_1 a_2 a_4^2 + a_5^3 a_4 + a_5 a_6^2 a_4 + a_5 a_7^2 a_4 + a_5 a_8^2 a_4 + 2a_2^2 a_5 a_4 + a_3^2 a_5 a_4 - a_5 a_4 - a_2 a_3 a_6 a_4 + a_1 a_3 a_7 a_4 - \frac{a_2 a_6 a_8 a_4}{\sqrt{3}}$$
$$+ \frac{a_1 a_7 a_8 a_4}{\sqrt{3}} - a_1 a_2 a_5^2 - \frac{1}{3}a_6 a_7 a_8^2 + a_1 a_3 a_5 a_6 + a_2 a_3 a_5 a_7 - a_3^2 a_6 a_7 - a_6 a_7 + \frac{a_1 a_5 a_6 a_8}{\sqrt{3}} + \frac{a_2 a_5 a_7 a_8}{\sqrt{3}} - \frac{2a_3 a_6 a_7 a_8}{\sqrt{3}},$$

$$a_{68} = \frac{1}{2}\sqrt{3}a_1 a_4^3 + \frac{1}{2}\sqrt{3}a_2 a_5 a_4^2 - 2a_6 a_8 a_4^2 + \frac{1}{2}\sqrt{3}a_1 a_5^2 a_4 + \frac{3}{2}\sqrt{3}a_1 a_6^2 a_4 + \frac{1}{2}\sqrt{3}a_1 a_7^2 a_4 + \frac{2a_1 a_8^2 a_4}{\sqrt{3}} - \frac{1}{4}\sqrt{3}a_1 a_4$$
$$- \sqrt{3}a_2 a_6 a_7 a_4 + \frac{1}{2}\sqrt{3}a_2 a_5^3 - \sqrt{3}a_3 a_6^3 - 2a_6 a_8^3 + \frac{3}{2}\sqrt{3}a_2 a_5 a_6^2 + \frac{1}{2}\sqrt{3}a_2 a_5 a_7^2 - \sqrt{3}a_3 a_6 a_7^2 + \frac{2a_2 a_5 a_8^2}{\sqrt{3}}$$
$$- \frac{2a_3 a_6 a_8^2}{\sqrt{3}} - \frac{1}{4}\sqrt{3}a_2 a_5 + \frac{1}{4}\sqrt{3}a_3 a_6 + \sqrt{3}a_1 a_5 a_6 a_7 - 2a_6^3 a_8 - 2a_6 a_7^2 a_8 - 2a_5^2 a_6 a_8 + \frac{a_6 a_8}{4},$$

$$
\begin{aligned}
a_{77} &= a_5^4 + a_2^2a_5^2 + a_3^2a_5^2 + a_4^2a_5^2 + a_6^2a_5^2 + a_7^2a_5^2 + a_8^2a_5^2 - a_5^2 + 2a_1a_2a_4a_5 + 2a_1a_3a_7a_5 + \frac{2a_1a_7a_8a_5}{\sqrt{3}} - a_2^2a_4^2 \\
&\quad - \frac{a_6^2}{4} - a_3^2a_7^2 - \frac{5a_7^2}{4} - \frac{1}{3}a_7^2a_8^2 - \frac{a_8^2}{6} - 2a_2a_3a_4a_7 - \frac{2a_3a_7^2a_8}{\sqrt{3}} + \frac{a_3a_8}{2\sqrt{3}} - \frac{2a_2a_4a_7a_8}{\sqrt{3}} + \frac{1}{4}, \\
a_{78} &= -\frac{1}{2}\sqrt{3}a_2a_4^3 + \frac{1}{2}\sqrt{3}a_1a_5a_4^2 - 2a_7a_8a_4^2 - \frac{1}{2}\sqrt{3}a_2a_5^2a_4 - \frac{1}{2}\sqrt{3}a_2a_6^2a_4 - \frac{3}{2}\sqrt{3}a_2a_7^2a_4 - \frac{2a_2a_8^2a_4}{\sqrt{3}} + \frac{1}{4}\sqrt{3}a_2a_4 \\
&\quad + \sqrt{3}a_1a_6a_7a_4 + \frac{1}{2}\sqrt{3}a_1a_5^3 - \sqrt{3}a_3a_7^3 - 2a_7a_8^3 + \frac{1}{2}\sqrt{3}a_1a_5a_6^2 + \frac{3}{2}\sqrt{3}a_1a_5a_7^2 + \frac{2a_1a_5a_8^2}{\sqrt{3}} - \frac{2a_3a_7a_8^2}{\sqrt{3}} \\
&\quad - \frac{1}{4}\sqrt{3}a_1a_5 - \sqrt{3}a_3a_6^2a_7 + \frac{1}{4}\sqrt{3}a_3a_7 + \sqrt{3}a_2a_5a_6a_7 - 2a_7^3a_8 - 2a_5^2a_7a_8 - 2a_6^2a_7a_8 + \frac{a_7a_8}{4}, \\
a_{88} &= -\frac{3a_4^4}{4} - \frac{3}{2}a_5^2a_4^2 - \frac{3}{2}a_6^2a_4^2 - \frac{3}{2}a_7^2a_4^2 - 2a_8^2a_4^2 + \frac{3a_4^2}{4} - \frac{3a_5^4}{4} - \frac{3a_6^4}{4} - \frac{3a_7^4}{4} - \frac{4a_8^4}{3} \\
&\quad + \frac{3a_5^2}{4} - \frac{3}{2}a_5^2a_6^2 + \frac{3a_6^2}{4} - \frac{3}{2}a_5^2a_7^2 - \frac{3}{2}a_6^2a_7^2 + \frac{3a_7^2}{4} - 2a_5^2a_8^2 - 2a_6^2a_8^2 - 2a_7^2a_8^2.
\end{aligned}
$$

Note that, because of the symmetry of the Hamiltonian, $a_{ij} = a_{ji}$.

In contrast to the qubit case where such expressions are simple and intuitive, the long expressions in the qutrit case are hard to use directly. The complexity of these expressions shows that Theorem 3.1 is not a trivial statement, despite it being straightforward in the qubit case.

APPENDIX B: DETAILS OF PULSE SEQUENCES AND FRAME SETS

1. Details of qutrit decoupling frame sets

In this appendix, we utilize the linear programming formulation described in Ref. [22] to identify promising candidates for frame sets.

Before discussing the details, let us first comment on the existence of some equivalence relations between distinct frame sets, in close relation to the results in Appendix A 5. Consider the frames formed by conjugating by pulses P_1 and P_2:

$$S_1 = P_1^\dagger S^z P_1, \qquad S_2 = P_1^\dagger P_2^\dagger S^z P_2 P_1. \tag{B1}$$

Then, a further conjugation by U would give rise to

$$S_1' = U^\dagger P_1^\dagger S^z P_1 U, \qquad S_2' = U^\dagger P_1^\dagger P_2^\dagger S^z P_2 P_1 U. \tag{B2}$$

However, physically speaking, we could regard U as an initial-state preparation pulse. The subsequent decoupling pulses will then be unaffected, and therefore, from the perspective of the average Hamiltonian, the two sequences are equivalent.

Given this equivalence, when performing calculations, it may be convenient to conjugate the whole pulse set by the same unitary $P_1^\dagger$, in order to start with the frame S^z. This method will also allow us to analyze different pulse sequences on a more equal footing. Moreover, this process helps to prevent potential confusion in analyzing pulse sequences related to the order of conjugations when applying a pulse sequence. For example, it may appear that the Gell-Mann basis λ_1 can be transformed into λ_4 by a cyclic echo pulse P_c (see Appendix B 3 for the definition), in the sense that $P_c^\dagger \lambda_1 P_c = \lambda_4$; however, in fact, if one starts in the frame $S_1 = \lambda_1 = P_1^\dagger S^z P_1$, then the cyclic echo pulse P_c will not bring one to the frame λ_4, i.e., $P_1^\dagger P_c^\dagger S^z P_c P_1 \neq \lambda_4$, since the new pulse acts from the middle instead of being added at the ends.

After imposing that one starts with the frame S^z, there is still an additional degree of freedom to conjugate pulse sequences, namely, a conjugation of all frames by a diagonal phase rotation. This process will give rise to a family of frame configurations that are distinct but can be related to each other. Moreover, if one member of this family can be implemented with some set of elementary pulses composed of resonant driving on one or both magnetically allowed transitions, the pulses necessary to implement a different member of this family can be easily obtained by changing the phase of the original pulses. This finding could be useful in performing additional symmetrization of a pulse sequence to further improve its performance and cancel higher-order terms.

We now describe some of the promising frame sets that were found. By allowing $\pi/2$ driving pulses on all three transitions, including the magnetically forbidden transition, we found that the following 12 frames with equal time duration achieve full disorder and interaction decoupling:

$$\begin{pmatrix} 0 & 0 & 0 \\ 0 & 0 & \pm 1 \\ 0 & \pm 1 & 0 \end{pmatrix}, \quad \begin{pmatrix} 0 & 0 & 0 \\ 0 & 0 & \pm i \\ 0 & \mp i & 0 \end{pmatrix}, \quad \begin{pmatrix} 0 & 0 & \pm 1 \\ 0 & 0 & 0 \\ \pm 1 & 0 & 0 \end{pmatrix},$$
$$\begin{pmatrix} 0 & 0 & \pm i \\ 0 & 0 & 0 \\ \mp i & 0 & 0 \end{pmatrix}, \quad \begin{pmatrix} 0 & \pm 1 & 0 \\ \pm 1 & 0 & 0 \\ 0 & 0 & 0 \end{pmatrix}, \quad \begin{pmatrix} 0 & \pm i & 0 \\ \mp i & 0 & 0 \\ 0 & 0 & 0 \end{pmatrix}. \tag{B3}$$

This frame set does not contain S^z as an element. Therefore, based on the preceding discussion, we can perform a global unitary rotation to bring this frame set into the following form (alternatively, it can also be directly found by performing linear programming with a pulse set composed purely of balanced double-driving pulses):

$$\pm S^x = \pm \frac{1}{\sqrt{2}} \begin{pmatrix} 0 & 1 & 0 \\ 1 & 0 & 1 \\ 0 & 1 & 0 \end{pmatrix}, \quad \pm S^{\tilde{x}} = \pm \frac{1}{\sqrt{2}} \begin{pmatrix} 0 & 1 & 0 \\ 1 & 0 & -1 \\ 0 & -1 & 0 \end{pmatrix},$$
$$\pm S^y = \pm \frac{1}{\sqrt{2}} \begin{pmatrix} 0 & -i & 0 \\ i & 0 & -i \\ 0 & i & 0 \end{pmatrix}, \quad \pm S^{\tilde{y}} = \pm \frac{1}{\sqrt{2}} \begin{pmatrix} 0 & -i & 0 \\ i & 0 & i \\ 0 & -i & 0 \end{pmatrix},$$
$$\pm S^z = \pm \begin{pmatrix} 1 & 0 & 0 \\ 0 & 0 & 0 \\ 0 & 0 & -1 \end{pmatrix}, \quad \pm S^{\tilde{z}} = \pm \begin{pmatrix} 0 & 0 & -i \\ 0 & 0 & 0 \\ i & 0 & 0 \end{pmatrix}. \tag{B4}$$

This is the basic frame set that we use for the majority of our qutrit decoupling pulse sequences. Note that by globally changing the phases of all rotations, we can also generate other equivalent classes of frames. In addition, note that another way to specify these frames is to specify them as commutators and anticommutators of spin-1 operators:

$$S^{(x,y,z)} \propto [S^\mu, S^\nu],$$
$$S^{(\tilde{x},\tilde{y},\tilde{z})} \propto \{S^\mu, S^\nu\}, \tag{B5}$$

with $\mu, \nu \in \{x, y, z\}$, which generate the irreducible representations of SU(2) discussed in Ref. [72].

Another example frame set that was identified with these methods is

$$\begin{pmatrix} 0 & \frac{1}{\sqrt{2}} & 0 \\ \frac{1}{\sqrt{2}} & 0 & -\frac{1}{\sqrt{2}} \\ 0 & -\frac{1}{\sqrt{2}} & 0 \end{pmatrix}, \quad \begin{pmatrix} 0 & \frac{i}{\sqrt{2}} & 0 \\ -\frac{i}{\sqrt{2}} & 0 & -\frac{i}{\sqrt{2}} \\ 0 & \frac{i}{\sqrt{2}} & 0 \end{pmatrix}, \quad \begin{pmatrix} -\frac{1}{2} & 0 & -\frac{1}{2} \\ 0 & 1 & 0 \\ -\frac{1}{2} & 0 & -\frac{1}{2} \end{pmatrix},$$
$$\begin{pmatrix} 0 & \frac{i}{\sqrt{2}} & 0 \\ -\frac{i}{\sqrt{2}} & 0 & \frac{1}{\sqrt{2}} \\ 0 & \frac{1}{\sqrt{2}} & 0 \end{pmatrix}, \quad \begin{pmatrix} 0 & \frac{i}{\sqrt{2}} & 0 \\ -\frac{i}{\sqrt{2}} & 0 & -\frac{1}{\sqrt{2}} \\ 0 & -\frac{1}{\sqrt{2}} & 0 \end{pmatrix}, \quad \begin{pmatrix} -\frac{1}{2} & 0 & -\frac{i}{2} \\ 0 & 1 & 0 \\ \frac{i}{2} & 0 & -\frac{1}{2} \end{pmatrix},$$
$$\begin{pmatrix} 0 & \frac{i}{\sqrt{2}} & 0 \\ -\frac{i}{\sqrt{2}} & 0 & \frac{i}{\sqrt{2}} \\ 0 & -\frac{i}{\sqrt{2}} & 0 \end{pmatrix}, \quad \begin{pmatrix} 0 & -\frac{i}{\sqrt{2}} & 0 \\ \frac{i}{\sqrt{2}} & 0 & \frac{i}{\sqrt{2}} \\ 0 & -\frac{i}{\sqrt{2}} & 0 \end{pmatrix}, \quad \begin{pmatrix} 0 & 0 & 0 \\ 0 & 1 & 0 \\ 0 & 0 & -1 \end{pmatrix},$$
$$\begin{pmatrix} 0 & -\frac{i}{\sqrt{2}} & 0 \\ \frac{i}{\sqrt{2}} & 0 & -\frac{1}{\sqrt{2}} \\ 0 & -\frac{1}{\sqrt{2}} & 0 \end{pmatrix}, \quad \begin{pmatrix} 0 & -\frac{i}{\sqrt{2}} & 0 \\ \frac{i}{\sqrt{2}} & 0 & \frac{1}{\sqrt{2}} \\ 0 & \frac{1}{\sqrt{2}} & 0 \end{pmatrix}, \quad \begin{pmatrix} -1 & 0 & 0 \\ 0 & 1 & 0 \\ 0 & 0 & 0 \end{pmatrix}, \tag{B6}$$

but we do not use this frame set in practice because its graph connectivity is considerably worse.

2. Details of qutrit decoupling pulse sequences

In this section, we describe in detail Seq. 2 (interaction decoupling), Seq. B (nonrobust decoupling), and Seq. C (DROID-C3PO), which we mentioned in Fig. 8(a).

Sequence 2 (interaction decoupling) is the interaction decoupling sequence designed in Ref. [22]. This sequence only decouples interactions but not disorder, so its performance is not expected to be good in our experimental platform of interacting NV ensembles because our system is disorder dominated. This pulse sequence is plotted in Fig. 12.

Sequence B (nonrobust decoupling) is the sequence plotted in Figs. 3(e) and 3(f), which go through the 12 frames in a somewhat arbitrary fashion. When spending

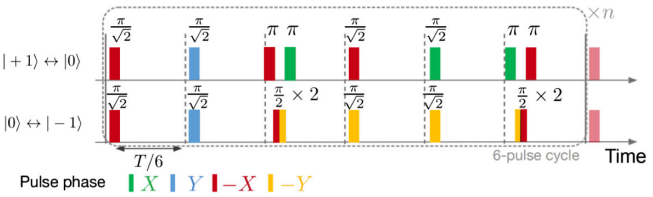

FIG. 12. Pulse-sequence "interaction decoupling." This sequence was proposed in Ref. [22].

FIG. 13. Frame representation of Seq. B (nonrobust decoupling). This sequence is the sequence plotted in Figs. 3(e) and 3(f), which is a nonrobust disorder and interaction decoupling sequence.

equal time in the 12 frames, the disorder and interaction decoupling sequence is not robust to finite-pulse-duration effects. The frame representation of this sequence is shown in Fig. 13.

Sequence C (DROID-C3PO) is our current best sequence whose design is discussed in Sec. IV. The sequence is plotted in Fig. 1(b), and its frame representation is shown in Fig. 14(a).

One subtle point about Seq. C is that it has a net π rotation in each Floquet period. Namely, the unitary due to the pulses in each Floquet period is

$$\hat{U} = \begin{pmatrix} -1 & 0 & 0 \\ 0 & 1 & 0 \\ 0 & 0 & -1 \end{pmatrix}. \tag{B7}$$

This net rotation has the potential advantage that the frames in two neighboring Floquet periods are not exactly the same; therefore, it allows further cancellation between Floquet periods, but it also requires one to be careful because the net rotation changes the readout axis.

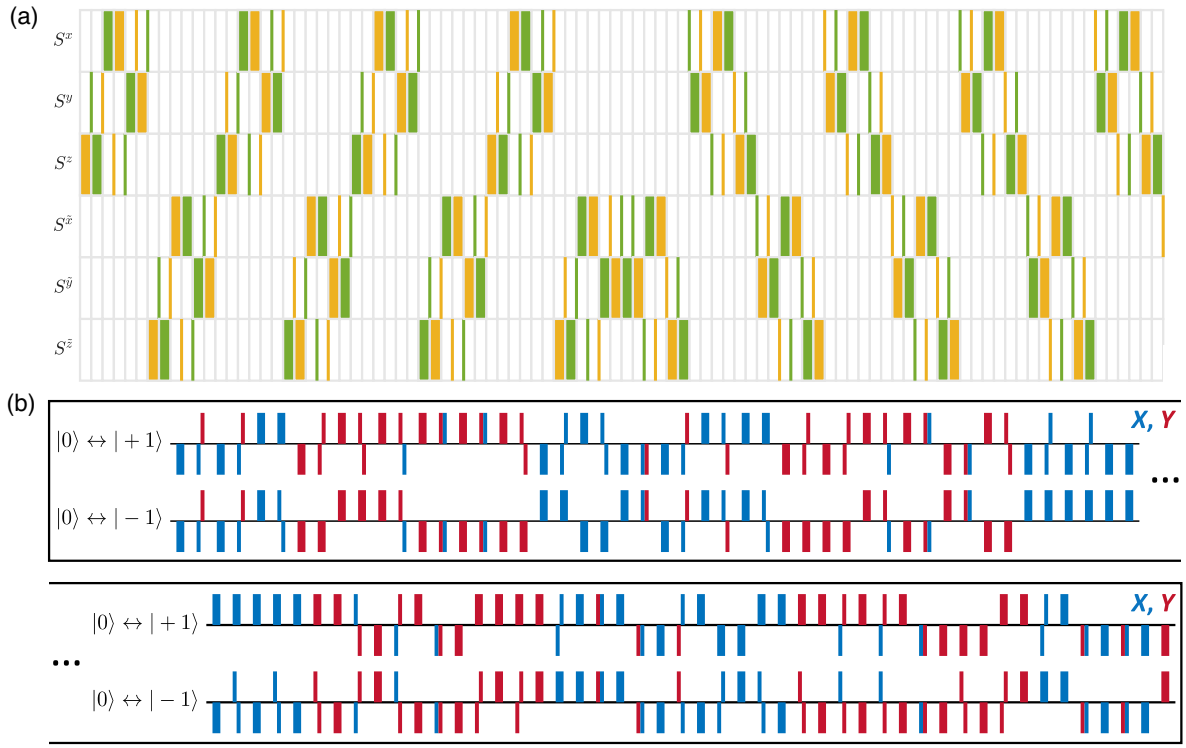

FIG. 14. Plot of Seq. C (DROID-C3PO). This sequence is our current best disorder and interaction decoupling sequence. It is robust to disorder during pulses and rotation angle errors in both transitions, and also cancels some higher-order terms in the Magnus expansion. (a) Frame representation of this sequence. The yellow and green colors represent plus and minus signs of the frames, and the thick and thin lines represent free evolution frames and intermediate frames during pulses, respectively. The sequence is built from the building blocks in Fig. 5(c), which are repeated 8 times with different sign and ordering choices to further cancel the $(S^z)^2$ disorder during the pulses, the Rabi inhomogeneity effect, and the first-order terms in the Magnus expansion. See Ref. [74] for more details on this symmetrization strategy. (b) Actual pulses constituting this sequence. All pulses in this sequence are balanced double driving. The thin lines represent spin-1 $\pi/2$ pulses (i.e., rotation of the spin-1 generalized Bloch sphere by an angle $\pi/2$, experimentally implemented by simultaneously driving the two transitions with two $\pi/\sqrt{2}$ pulses), and the thick lines represent spin-1 π pulses. The colors of the pulses represent the pulse axis (X or Y), and the direction of the pulses (up or down) represent the two opposite rotation directions (e.g., the $+\pi/2$ pulse and the $-\pi/2$ pulse). The proportions of this plot are drawn consistently with actual time durations. The ellipsis in the plot indicates that the two rows are connected. The plot is identical to Fig. 1(b), repeated here for convenience.

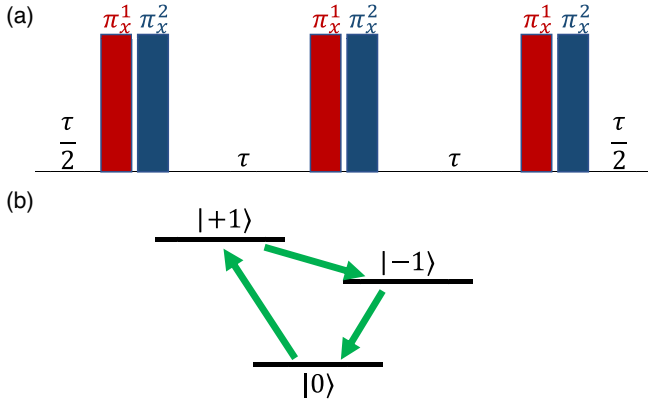

FIG. 15. Plot of cyclic echo. (a) The cyclic echo consists of three pairs of π pulses as shown in the plot. The pulses π_x^1 and π_x^2 represent a π pulse around the x axis for the transition $|0\rangle \leftrightarrow |+1\rangle$ and the transition $|0\rangle \leftrightarrow |-1\rangle$, respectively. (b) Each pair of π pulses in diagram (a) causes a cyclic permutation of the three states (as shown by the green arrows); therefore, the disorder is averaged out by this sequence.

3. Robust disorder decoupling

In this section, we describe the disorder decoupling sequences, Seq. 1 (cyclic echo) and Seq. A (robust cyclic echo) that we mentioned in Fig. 8(a).

Sequence 1 (cyclic echo) is the simplest sequence that allows one to decouple the on-site disorder. This sequence is plotted in Fig. 15, and it works by cyclically permutating the three states $|+1\rangle$, $|0\rangle$, and $|-1\rangle$ to average out the disorder.

Sequence A (robust cyclic echo) is a sequence built on the cyclic echo that decouples disorder and is robust to finite pulse effects and Rabi inhomogeneity. This sequence consists of two iterations of cyclic echo, where the phase of pulses in the second iteration is adjusted to $(-\pi_x^1, \pi_x^2, \pi_x^1, -\pi_x^2, -\pi_x^1, \pi_x^2)$. The way this sequence cancels the disorder during the pulses is by a simple one-to-one cancellation between the two iterations, which is not hard to verify explicitly. For optimization of performance, we further symmetrize the sequence by adding a free evolution time τ between the pairs of π pulses in Fig. 15(a), which changes the cyclic permutation of the three levels shown in Fig. 15(b) into a full permutation. This sequence also shares the same net π rotation in each Floquet period as discussed in Appendix B 2.

4. Derivation for disorder effects during pulses

In this section, we discuss how disorder transforms during pulses, which is essential to understand for designing sequences robust to it.

Before going into the details for the spin-1 case, we note the simple geometric picture in the spin-$\frac{1}{2}$ case. In the spin-$\frac{1}{2}$ case, as we already discussed in the main text, an on-resonance pulse leads to an S^z operator trajectory that

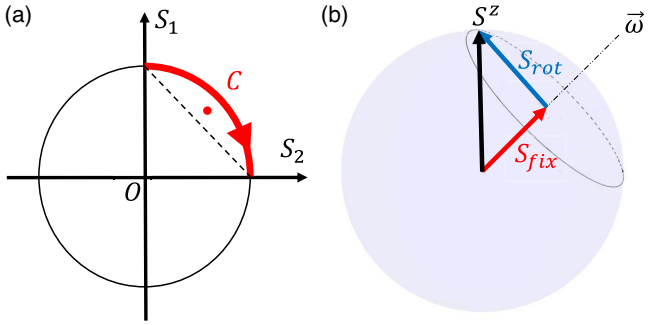

FIG. 16. Transformation of S^z during pulses. (a) When the trajectory of S^z lives on a geodesic, its transformation during the pulse is a simple rotation from its initial position S_1 to its final position S_2, as shown by the red arc. Then, the averaged S^z operator during the pulse is represented by the center of mass of the red arc. From the plot, we can see that the averaged S^z operator can be decomposed as a simple average of S_1 and S_2, and the extra $4/\pi$ factor in Eq. (B8) comes from the fact that the center of mass of the red curve is slightly further from the origin O compared to the midpoint between S_1 and S_2. The plot is identical to Fig. 4(a), repeated here for convenience. (b) When the trajectory of S^z lives in a two-dimensional slice that does not go through the origin (as shown by the black circle in the plot), $\tilde{S}^z(t)$ can be decomposed into an invariant part S_{fix} during the pulse and a part S_{rot} that rotates on a circle, with the latter's averaged effect following the same rule as in plot (a).

transforms along a geodesic on the Bloch sphere [represented by the red arc in Fig. 4(a) and repeated here in Fig. 16(a) for convenience]. As a result, the averaged effect of disorder during the pulse, as represented by the center of mass of the red arc in Fig. 16(a), can be decomposed as an average of the frames before and after the pulse:

$$\bar{S} = \frac{4}{\pi}\left[\frac{S_1 + S_2}{2}\right], \tag{B8}$$

where the factor $\frac{4}{\pi}$ comes from the fact that the center of mass is slightly further from the origin than the midpoint between S_1 and S_2.

Even if the pulse is not on resonance, the story does not change too much because the trajectory of the S^z operator on the Bloch sphere is still a circle (the only difference is that now the circle is not a geodesic on the Bloch sphere). In this case, the evolution of the S^z operator can be decomposed into two parts as shown in Fig. 16(b): The first part is the projection of S^z on the rotation axis, which is invariant during the pulse; the remaining part rotates on a circle perpendicular to the rotation axis, and therefore, its effect during the pulse can be decomposed as a linear combination before and after the pulse, similar to the case in Fig. 16(a).

Although the geometric picture in the spin-$\frac{1}{2}$ case is very simple (the trajectory of the S^z operator is always a circle), the trajectory of the S^z operator in the spin-1 case can be much more complicated. To see this, let us consider the

trajectory of the S^z operator transformed by a generic Hamiltonian H:

$$\tilde{S}^z(t) = e^{iHt} S^z e^{-iHt}. \tag{B9}$$

Generically, the conjugation of the SU(3) operator e^{-iHt} on S^z leads to a rotation on an eight-dimensional sphere, which is the spin-1 generalization of the Bloch sphere (the coordinates on the eight-dimensional sphere are the expansion coefficients of $\tilde{S}^z$ in the Gell-Mann basis; see Refs. [22,67] for more details). In order to analyze the trajectory of $\tilde{S}^z(t)$ on this eight-dimensional sphere, let us calculate its time derivatives at $t = 0$:

$$\begin{aligned} \tilde{S}^z|_{t=0} &= S^z, \\ \frac{d}{dt}\tilde{S}^z|_{t=0} &= [iH, S^z], \\ \frac{d^2}{dt^2}\tilde{S}^z|_{t=0} &= [iH, [iH, S^z]], \\ &\cdots \end{aligned} \tag{B10}$$

From the above expression, we know that the trajectory of $\tilde{S}^z(t)$ lives in a subspace spanned by $\{[iH, S^z], [iH, [iH, S^z]], ...\}$. Therefore, the number of linearly independent matrices in the set $\{[iH, S^z], [iH, [iH, S^z]], ...\}$ is the dimension of the subspace that the trajectory of $\tilde{S}^z(t)$ lives in.

By calculating the rank of the above set for randomly chosen H, we know that for generic pulses, the dimension of the subspace is 6. Even when we restrict the pulses to be on resonance, the dimension is still 4. Therefore, the trajectory of $\tilde{S}^z(t)$ is very complicated in the generic case, and there is no simple expression for the disorder during pulses. However, we can still obtain useful results in certain special cases:

(i) Most importantly, as we already discussed in the main text, when the pulse is a balanced double-driving pulse (i.e., simultaneously driving the two magnetically allowed transitions with equal amplitude), the trajectory of the S^z operator becomes a geodesic, and therefore, all of the nice properties in the spin-$\frac{1}{2}$ case are recovered. This finding is the key insight that allows us to elegantly cancel the disorder during pulses.

(ii) When the pulse is a resonant driving on a single transition, the trajectory of S^z can be decomposed into a fixed part and a rotating part similar to Fig. 16(b). To see this case, consider a pulse applied on the $|0\rangle \leftrightarrow |-1\rangle$ transition. In this case, we can explicitly decompose S^z as

$$S^z = \begin{pmatrix} 1 & 0 & 0 \\ 0 & 0 & 0 \\ 0 & 0 & -1 \end{pmatrix} = \begin{pmatrix} 1 & 0 & 0 \\ 0 & -\frac{1}{2} & 0 \\ 0 & 0 & -\frac{1}{2} \end{pmatrix} + \begin{pmatrix} 0 & 0 & 0 \\ 0 & \frac{1}{2} & 0 \\ 0 & 0 & -\frac{1}{2} \end{pmatrix}, \tag{B11}$$

where the first term is invariant under the rotation and the second term rotates as a spin-$\frac{1}{2}$ S^z operator during the pulse. If the pulse is a $\pi/2$ pulse, then the average effect of the second term during the pulse is given by Eq. (B8), and the average effect of the first term is simply itself. Because of the extra coefficient $4/\pi$ that only appears for the second term, when the two terms are summed together, their average effect is no longer a simple average before and after the pulse. This finding is a concrete example that shows the complication in the qudit case compared to the qubit case.

(iii) Although the trajectory of $\tilde{S}^z$ is very complicated for generic on-resonance pulses, the trajectory of $(\tilde{S}^z)^2$ always lives in a two-dimensional space [i.e., looks like the trajectory in Fig. 16(b)]. To see this case, notice that when $|0\rangle$ is coupled to $|+1\rangle$ and $|-1\rangle$ by on-resonance pulses, it can also be seen that $|0\rangle$ is coupled to a bright state $|B\rangle$ while leaving a dark state $|D\rangle$ not coupled to anything. For convenience, we can perform a basis transformation from $\{|0\rangle, |+1\rangle, |-1\rangle\}$ to $\{|0\rangle, |B\rangle, |D\rangle\}$. Since $(S^z)^2$ is the identity in the $\{|+1\rangle, |-1\rangle\}$ subspace, it is invariant under this basis transformation. Working in this bright- and dark-state basis, since $|0\rangle$ is only coupled to $|B\rangle$, the transformation of $(S^z)^2$ is kept block diagonal, with one block (corresponding to $|D\rangle$) invariant and the other block (corresponding to $\{|0\rangle, |B\rangle\}$) transforming as a two-level system. Therefore, the trajectory of $(\tilde{S}^z)^2$ can be decomposed into a fixed part and a rotating part, as shown in Fig. 16(b). As a specific example, for a spin-1 $\pi/2$ pulse,

$$U_p = \exp\left[-i\begin{pmatrix} 0 & \theta_1 + i\theta_2 & 0 \\ \theta_1 - i\theta_2 & 0 & \theta_3 + i\theta_4 \\ 0 & \theta_3 - i\theta_4 & 0 \end{pmatrix}\right], \tag{B12}$$

with $\theta_1^2 + \theta_2^2 + \theta_3^2 + \theta_4^2 = \theta_{\text{tot}}^2 = \pi^2/4$; the averaged $(S^z)^2$ operator during this pulse is

$$\bar{S} = \frac{4}{\pi}\left[\frac{(S_1^2 - S_{\text{fix}}) + (S_2^2 - S_{\text{fix}})}{2}\right] + S_{\text{fix}}, \tag{B13}$$

where S_1 and S_2 are the frames before and after the pulse, and $S_{\text{fix}} = (1/2\pi)\int_0^{2\pi} d\theta U_p^\dagger(\theta)(S^z)^2 U_p(\theta)$ is the invariant part of $(S^z)^2$ during the pulse.

5. Analysis of rotation angle error

In this section, we show that the robust qutrit decoupling sequence we designed [see Fig. 14(a) for its frame representation] is not only robust to rotation angle errors

common to both transitions, as discussed in the main text, but also to rotation angle errors on each individual transition.

To see this case, examine Fig. 14(a), and note what was exactly done in the "further improvement" level in the hierarchy described in the main text. In the whole sequence DROID-C3PO, there are eight iterations of the basic disorder and interaction decoupling sequence shown in Fig. 5(c). The difference between the first four iterations is that signs of free evolution frames and intermediate frames are flipped. For two neighboring frames A and B, their signs go over all four possibilities (A,B), $(A,-B)$, $(-A,B)$, and $(-A,-B)$. The second four iterations are obtained by flipping both the signs and the ordering of the frames in the first four iterations [74]. Because of the structure discussed above, for any neighboring frames (A,B) in the first four iterations, there is a pair of frames $(-A,-B)$ in the first four iterations, and therefore, there is a pair of frames (B,A) in the second four iterations. Because the rotation from frame B to frame A is exactly the reverse rotation from A to B, the rotation angle error on each individual transition is canceled between frame pairs (A,B) in the first four iterations and (B,A) in the second four iterations. Thus, we see how rotation angle errors on each individual transition are canceled in the sequence.

6. Geometric intuition of scar subspace

In this section, we discuss the geometric structure of the scar subspace $|S_n\rangle$ as defined in Eq. (13). When restricted to the subspace spanned by $|+1\rangle$ and $|-1\rangle$, the operator $\frac{1}{2}(S_i^+)^2$ becomes the spin-$\frac{1}{2}$ raising operator. If we further rotate the spins in the second group by π around the z axis, this raising operator will flip its sign (because the signs of S^x and S^y are flipped), and the operator J^+ will become exactly the many-body raising operator. Since the state $|\Omega\rangle$ is the state $|S=(N/2), m_S=-(N/2)\rangle$, the states $|S_n\rangle$ will be $|S=(N/2), m_S=-(N/2)+n\rangle$ after rotating the spins in the second group by π around the z axis. Therefore, the subspace spanned by $|S_n\rangle$ is the maximal spin subspace after rotating the second group by π around the z axis.

7. Decoupling with nongeodesic pulses

In this section, we show another robust qutrit disorder and interaction decoupling sequence whose frame set is different from the 12 frames shown in Fig. 3(e) and whose pulses do not lead to a geodesic trajectory of $\tilde{S}^z$ (see Sec. III C for the context of geodesics).

The basic idea of this sequence is also a hierarchical design: Since disorder is much stronger than interactions in our experimental platform, we want to robustly decouple disorder first and then decouple interactions on top of that. Therefore, we can use Seq. A (robust cyclic echo) (see Appendix B 3 for descriptions) as the inner layer to robustly decouple the disorder and, on top of that, design sequences to decouple the interaction transformed by the robust cyclic echo.

Because the robust cyclic echo sequence cyclically permutes the three energy levels, the form of the interaction is symmetrized under the transformation of this sequence. More concretely, the original interaction Hamiltonian, which only contains flip-flop terms between $|0\rangle \leftrightarrow |+1\rangle$ and between $|0\rangle \leftrightarrow |-1\rangle$, is transformed to

$$H'_{\mathrm{int}} = \frac{1}{2}S^z \otimes S^z + \frac{1}{2}S^z_\perp \otimes S^z_\perp - \frac{1}{3}H^{XY,+0} - \frac{1}{3}H^{XY,0-} - \frac{1}{3}H^{XY,+-}, \tag{B14}$$

where $H^{XY,ij} = \frac{1}{2}(X^{ij}\otimes X^{ij} + Y^{ij}\otimes Y^{ij})$ is the flip-flop term between state $|i\rangle$ and state $|j\rangle$, and $S^z_\perp$ is defined as

$$S^z_\perp \equiv \frac{1}{\sqrt{3}}\begin{pmatrix} 1 & 0 & 0 \\ 0 & -2 & 0 \\ 0 & 0 & 1 \end{pmatrix}. \tag{B15}$$

Using the framework we proposed in this paper, we found that the following 12 frames with equal time duration decouple the symmetrized interaction Eq. (B14):

$$S_1 = \begin{pmatrix} 0 & 1 & 0 \\ 1 & 0 & 0 \\ 0 & 0 & 0 \end{pmatrix}, \quad S_2 = \begin{pmatrix} 0 & 0 & 0 \\ 0 & 0 & 1 \\ 0 & 1 & 0 \end{pmatrix},$$
$$S_3 = \begin{pmatrix} 0 & -i & 0 \\ i & 0 & 0 \\ 0 & 0 & 0 \end{pmatrix}, \quad S_4 = \begin{pmatrix} 0 & 0 & 0 \\ 0 & 0 & -i \\ 0 & i & 0 \end{pmatrix},$$
$$S_5 = \frac{1}{\sqrt{2}}\begin{pmatrix} 0 & 1 & 0 \\ 1 & 0 & 1 \\ 0 & 1 & 0 \end{pmatrix}, \quad S_6 = \frac{1}{\sqrt{2}}\begin{pmatrix} 0 & 1 & 0 \\ 1 & 0 & -1 \\ 0 & -1 & 0 \end{pmatrix},$$
$$S_7 = \frac{1}{\sqrt{2}}\begin{pmatrix} 0 & -i & 0 \\ i & 0 & -i \\ 0 & i & 0 \end{pmatrix}, \quad S_8 = \frac{1}{\sqrt{2}}\begin{pmatrix} 0 & -i & 0 \\ i & 0 & i \\ 0 & -i & 0 \end{pmatrix},$$
$$S_9 = \frac{1}{\sqrt{2}}\begin{pmatrix} 0 & -i & 0 \\ i & 0 & 1 \\ 0 & 1 & 0 \end{pmatrix}, \quad S_{10} = \frac{1}{\sqrt{2}}\begin{pmatrix} 0 & -i & 0 \\ i & 0 & -1 \\ 0 & -1 & 0 \end{pmatrix},$$
$$S_{11} = \frac{1}{\sqrt{2}}\begin{pmatrix} 0 & 1 & 0 \\ 1 & 0 & -i \\ 0 & i & 0 \end{pmatrix}, \quad S_{12} = \frac{1}{\sqrt{2}}\begin{pmatrix} 0 & 1 & 0 \\ 1 & 0 & i \\ 0 & -i & 0 \end{pmatrix}. \tag{B16}$$

The connectivity of these 12 frames by experimental pulses is shown in Fig. 17. As the figure shows, these 12 frames can be connected by balanced double-driving (i.e., equal driving amplitude on the two allowed transitions) $\pi/4$

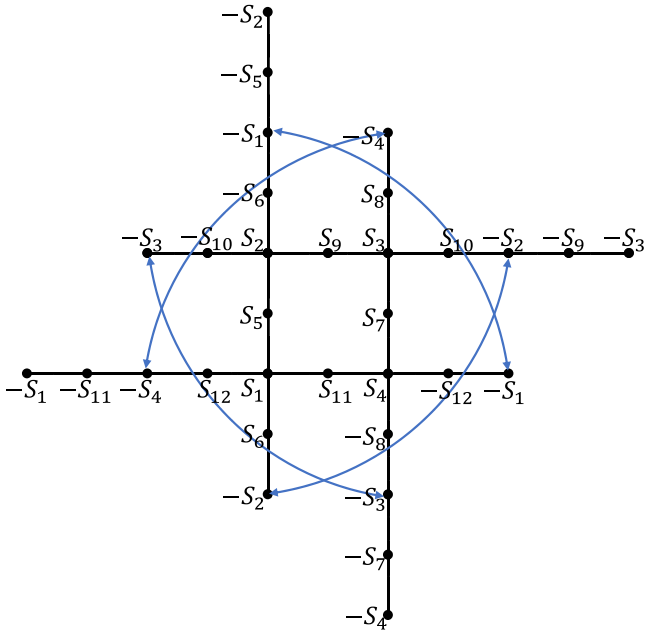

FIG. 17. Connectivity graph of the 12 frames in Eq. (B16). Each vertex represents one frame, and each segment represents a balanced double-driving $\pi/4$ pulse. The four straight lines represent four geodesics on which frames can be transformed to each other by repeating the same spin-1 $\pi/4$ pulse. Notice that vertices with the same label represent the same frame. For convenience, four pairs of identical frames are connected by blue arcs.

pulses, which is easily implementable in experiments. The whole disorder and interaction decoupling sequence is made of 12 iterations of robust cyclic echo, with the double-driving $\pi/4$ pulses connecting the above 12 frames inserted between neighboring iterations. A concrete example of such a sequence is given in Fig. 18. The sequence in Fig. 18 is nearly robust to disorder during pulses because the disorder during the pulses in each iteration of the robust cyclic echo is canceled. Although the disorder during the $\pi/4$ pulses connecting the above 12 frames is not canceled, it does not matter too much because these pulses take only a very small fraction of time in the whole sequence. Finally, we note that there are at least three ways to further improve the performance of the sequence in Fig. 18:

(i) We can further symmetrize the robust cyclic echo by adding a free evolution time τ between the pair of π pulses constituting the cyclic echo, just as in Seq. A.

(ii) The sequence can in fact be made fully robust to disorder during pulses: We can compensate for disorder during the balanced double-driving $\pi/4$ pulses by slightly adjusting the free evolution times inside neighboring iterations of robust cyclic echo.

(iii) Nearly all pulses in the sequence in Fig. 18 are along the X axis, so there is potential space for further improvements by utilizing pulses along the Y axis.

APPENDIX C: DISCUSSIONS ON DROID-C3PO

1. Remaining decoherence mechanisms

In this section, we discuss the possible remaining decoherence mechanisms in DROID-C3PO, which we observed to have a coherence time of 4 μs in Fig. 8(a).

The remaining decoherence mechanisms can be divided into two categories: one intrinsic to the many-body system, and the other coming from external noise or experimental imperfections. The intrinsic part contributes about half of the observed decay, characterized by numerical simulations including dipolar interactions and static on-site disorder (see Fig. 19, blue trace). The dominant contribution to this part comes from residual interactions during pulses since

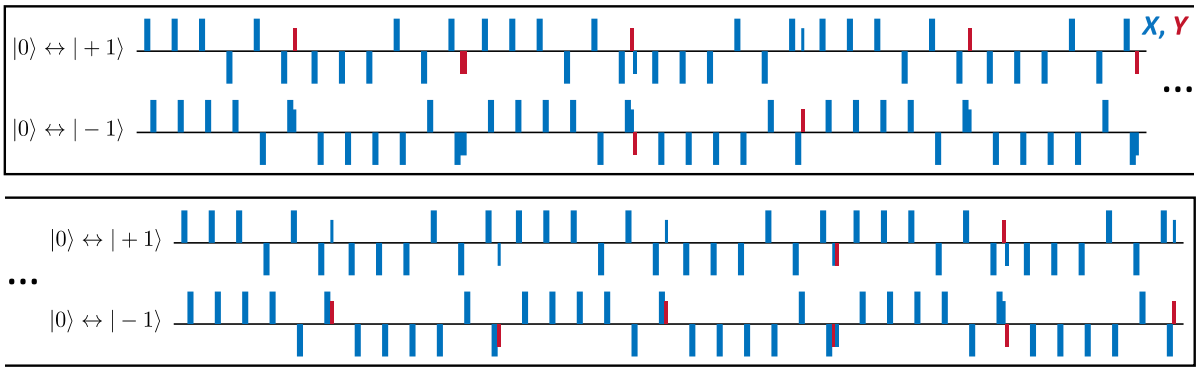

FIG. 18. Nongeodesic decoupling pulse sequence. There are two different types of pulses in this pulse sequence. One type of pulse is the π pulse on a single transition, represented by the taller pulses in the plot; these pulses constitute the robust cyclic echo, which decouples disorder robustly and locally. The other type of pulse is the balanced double-driving $\pi/4$ or $\pi/2$ pulse connecting the frames in Fig. 17, represented by the shorter pulses in the plot; these pulses further decouple interactions on top of disorder decoupling building blocks. The colors of the pulses represent the pulse axis (X or Y), and the direction of the pulses (up or down) represent the two opposite rotation directions (e.g., the $+\pi/2$ pulse and the $-\pi/2$ pulse). The proportion of this plot is drawn consistently with the actual time duration. The ellipsis in the plot shows that the two rows are connected.

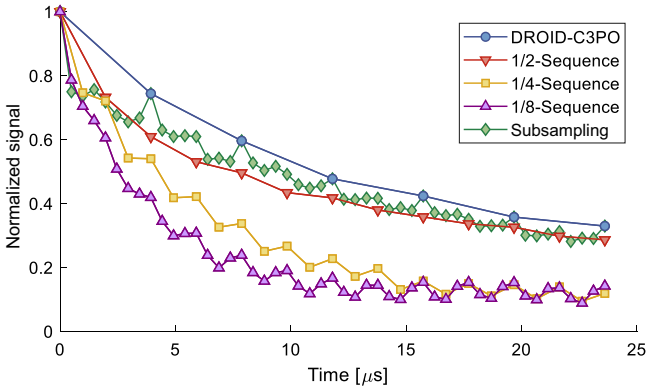

FIG. 19. Trade-off between sequence length and decoupling performance. The sequences being compared include DROID-C3PO [see Fig. 14(a)]; its first half, first $\frac{1}{4}$, and first $\frac{1}{8}$; and the subsampling method discussed in Appendix C 2. We see that the decoupling performance improves as we include more and more levels of symmetrization in the sequence, which serves to cancel $(S^z)^2$ disorder during pulses and higher-order terms in the Magnus expansion, as discussed in Sec. IV. 4. We also see that the subsampling method offers the opportunity for more observational windows without significant degradation of the decoupling performance. The oscillations in the yellow and purple traces come from the fact that the unitary implemented by the whole sequence is not the identity (see Appendix B 2 for more examples of this phenomenon). This case leads to different frame representations in neighboring Floquet periods, which cause accidental cancellation of certain terms, even though the pulses in the two Floquet periods are exactly the same. The peaks in the green trace correspond to those time points at which integer numbers of DROID-C3PO are implemented.

the sequence is only robust to disorder during pulses but not against interactions during pulses. This effect can potentially be reduced by decreasing the proportion of time during pulses or by carefully designing better sequences that are robust to interactions during pulses as well.

The other half of the decay is attributed to extrinsic sources, and we believe it mainly comes from the presence of dynamical disorder. In our spin-$\frac{1}{2}$ decoupling sequences, dynamical disorder limits us to a coherence time of 16 μs, so it is not unexpected that the same mechanism can give us an 8-μs extrinsic decay time in the spin-1 case, where the sensitivity to magnetic noise is twice that of the spin-$\frac{1}{2}$ case. Decoupling faster should, in general, help to reduce the effect of dynamical disorder since the power spectrum of noise is typically a decreasing function of frequency. However, one will eventually be limited by pulse distortions and inaccurate synchronization between the $|0\rangle \leftrightarrow |+1\rangle$ and $|0\rangle \leftrightarrow |-1\rangle$ driving, which becomes more and more significant when the pulse duration and spacing become shorter and shorter. In our spin-$\frac{1}{2}$ case, we find a sweet spot at π pulse duration $t_\pi = 10$ ns and free evolution time $\tau = 25$ ns, so we believe our parameters $t_\pi = 16$ ns and $\tau = 25$ ns in the spin-1 case should be pretty close to the sweet spot as well. Another way one can potentially reduce dynamical disorder without encountering the pulse distortion problem is to go to low temperatures.

2. Trade-off between sequence length and decoupling performance

In Fig. 8(a), we see that the sequence DROID-C3PO has good coherence time, but the sequence duration is on the same order of magnitude as the coherence time itself, leaving only a few observational windows before the signal is gone. In this section, we discuss how to create more observational windows within the coherence time.

In general, there are many ways to obtain more observational windows within the coherence time, including obvious methods such as decoupling faster or using a less dense ensemble that has a longer coherence time. For fixed external conditions, we can still use what we refer to as "subsampling" to create more observational windows without significantly hurting the performance of the sequence [70].

The subsampling method is based on the fact that DROID-C3PO has the structure of eight similar building blocks, as shown in Fig. 14(a). Each of the building blocks is a decoupling sequence on its own, and their combination makes the decoupling performance even better. Thus, one does not have to wait until the end of the whole Floquet period to probe the system; instead, probing at the end of each building block is possible since the dominant contribution of disorder and interactions is already decoupled there. We emphasize that this subsampling method is better than directly using a shorter sequence such as the Floquet sequence being repeated because, in this subsampling method, we are still benefiting from the mutual cancellation between different building blocks; it is only the last few building blocks that are not paired up that lead to slight degradation of the performance. Numerical results comparing the performance of sequences with different lengths are shown in Fig. 19, confirming our intuition.

[1] D. J. Wineland, J. J. Bollinger, W. M. Itano, F. L. Moore, and D. J. Heinzen, *Spin squeezing and reduced quantum noise in spectroscopy*, Phys. Rev. A **46**, R6797 (1992).
[2] Masahiro Kitagawa and Masahito Ueda, *Squeezed spin states*, Phys. Rev. A **47**, 5138 (1993).
[3] Jian Ma, Xiaoguang Wang, C. P. Sun, and Franco Nori, *Quantum spin squeezing*, Phys. Rep. **509**, 89 (2011).
[4] A. Yu Kitaev, *Fault-tolerant quantum computation by anyons*, Ann. Phys. (N.Y.) **303**, 2 (2003).
[5] K. J. Satzinger *et al.*, *Realizing topologically ordered states on a quantum processor*, Science **374**, 1237 (2021).
[6] G. Semeghini, H. Levine, A. Keesling, S. Ebadi, T. T. Wang, D. Bluvstein, R. Verresen, H. Pichler, M. Kalinowski, R. Samajdar, A. Omran, S. Sachdev, A. Vishwanath,

M. Greiner, V. Vuletić, and M. D. Lukin, *Probing topological spin liquids on a programmable quantum simulator*, Science **374**, 1242 (2021).

[7] Sebastian Hild, Takeshi Fukuhara, Peter Schauß, Johannes Zeiher, Michael Knap, Eugene Demler, Immanuel Bloch, and Christian Gross, *Far-from-equilibrium spin transport in Heisenberg quantum magnets*, Phys. Rev. Lett. **113**, 147205 (2014).

[8] Paul Niklas Jepsen, Jesse Amato-Grill, Ivana Dimitrova, Wen Wei Ho, Eugene Demler, and Wolfgang Ketterle, *Spin transport in a tunable Heisenberg model realized with ultracold atoms*, Nature (London) **588**, 403 (2020).

[9] K. X. Wei, E. Magesan, I. Lauer, S. Srinivasan, D. F. Bogorin, S. Carnevale, G. A. Keefe, Y. Kim, D. Klaus, W. Landers, N. Sundaresan, C. Wang, E. J. Zhang, M. Steffen, O. E. Dial, D. C. McKay, and A. Kandala, *Quantum crosstalk cancellation for fast entangling gates and improved multi-qubit performance*, Phys. Rev. Lett. **129**, 060501 (2022).

[10] Immanuel Bloch, Jean Dalibard, and Sylvain Nascimbène, *Quantum simulations with ultracold quantum gases*, Nat. Phys. **8**, 267 (2012).

[11] I. M. Georgescu, S. Ashhab, and Franco Nori, *Quantum simulation*, Rev. Mod. Phys. **86**, 153 (2014).

[12] Ehud Altman *et al.*, *Quantum simulators: Architectures and opportunities*, PRX Quantum **2**, 017003 (2021).

[13] André Eckardt, *Colloquium: Atomic quantum gases in periodically driven optical lattices*, Rev. Mod. Phys. **89**, 011004 (2017).

[14] Marin Bukov, Luca D'Alessio, and Anatoli Polkovnikov, *Universal high-frequency behavior of periodically driven systems: From dynamical stabilization to Floquet engineering*, Adv. Phys. **64**, 139 (2015).

[15] N. Goldman and J. Dalibard, *Periodically driven quantum systems: Effective Hamiltonians and engineered gauge fields*, Phys. Rev. X **4**, 031027 (2014).

[16] Christian Schweizer, Fabian Grusdt, Moritz Berngruber, Luca Barbiero, Eugene Demler, Nathan Goldman, Immanuel Bloch, and Monika Aidelsburger, *Floquet approach to 2 lattice gauge theories with ultracold atoms in optical lattices*, Nat. Phys. **15**, 1168 (2019).

[17] Joonhee Choi, Hengyun Zhou, Helena S. Knowles, Renate Landig, Soonwon Choi, and Mikhail D. Lukin, *Robust dynamic Hamiltonian engineering of many-body spin systems*, Phys. Rev. X **10**, 031002 (2020).

[18] Ken Xuan Wei, Chandrasekhar Ramanathan, and Paola Cappellaro, *Exploring localization in nuclear spin chains*, Phys. Rev. Lett. **120**, 070501 (2018).

[19] Sebastian Geier, Nithiwadee Thaicharoen, Clément Hainaut, Titus Franz, Andre Salzinger, Annika Tebben, David Grimshandl, Gerhard Zürn, and Matthias Weidemüller, *Floquet Hamiltonian engineering of an isolated many-body spin system*, Science **374**, 1149 (2021).

[20] J. S. Waugh, L. M. Huber, and U. Haeberlen, *Approach to high-resolution NMR in solids*, Phys. Rev. Lett. **20**, 180 (1968).

[21] A. Ajoy, U. Bissbort, D. Poletti, and P. Cappellaro, *Selective decoupling and Hamiltonian engineering in dipolar spin networks*, Phys. Rev. Lett. **122**, 013205 (2019).

[22] Soonwon Choi, Norman Y. Yao, and Mikhail D. Lukin, *Dynamical engineering of interactions in qudit ensembles*, Phys. Rev. Lett. **119**, 183603 (2017).

[23] D. P. Burum and W. K. Rhim, *Analysis of multiple pulse NMR in solids. III*, J. Chem. Phys. **71**, 944 (1979).

[24] D. G. Cory, J. B. Miller, and A. N. Garroway, *Time-suspension multiple-pulse sequences: Applications to solid-state imaging*, J. Magn. Reson. **90**, 205 (1990).

[25] Terry Gullion, David B Baker, and Mark S Conradi, *New, compensated Carr-Purcell sequences*, J. Magn. Reson. **89**, 479 (1990).

[26] U. Haeberlen and J. S. Waugh, *Coherent averaging effects in magnetic resonance*, Phys. Rev. **175**, 453 (1968).

[27] W-K. Rhim, D. D. Elleman, and R. W. Vaughan, *Analysis of multiple pulse NMR in solids*, J. Chem. Phys. **59**, 3740 (1973).

[28] Lieven M. K. Vandersypen, Matthias Steffen, Gregory Breyta, Costantino S. Yannoni, Mark H. Sherwood, and Isaac L. Chuang, *Experimental realization of Shor's quantum factoring algorithm using nuclear magnetic resonance*, Nature (London) **414**, 883 (2001).

[29] E. L. Hahn, *Spin echoes*, Phys. Rev. **80**, 580 (1950).

[30] Lorenza Viola, Emanuel Knill, and Seth Lloyd, *Dynamical decoupling of open quantum systems*, Phys. Rev. Lett. **82**, 2417 (1999).

[31] Ruben Verresen, *Everything is a quantum Ising model*, arXiv:2301.11917.

[32] Michael Schecter and Thomas Iadecola, *Weak ergodicity breaking and quantum many-body scars in spin-1 XY magnets*, Phys. Rev. Lett. **123**, 147201 (2019).

[33] Jean-Yves Desaules, Ana Hudomal, Debasish Banerjee, Arnab Sen, Zlatko Papić, and Jad C. Halimeh, *Prominent quantum many-body scars in a truncated Schwinger model*, Phys. Rev. B **107**, 205112 (2023).

[34] Jean-Yves Desaules, Debasish Banerjee, Ana Hudomal, Zlatko Papić, Arnab Sen, and Jad C. Halimeh, *Weak ergodicity breaking in the Schwinger model*, Phys. Rev. B **107**, L201105 (2023).

[35] M. S. Blok, V. V. Ramasesh, T. Schuster, K. O'Brien, J. M. Kreikebaum, D. Dahlen, A. Morvan, B. Yoshida, N. Y. Yao, and I. Siddiqi, *Quantum information scrambling on a superconducting qutrit processor*, Phys. Rev. X **11**, 021010 (2021).

[36] Emily J. Davis, Gregory Bentsen, Lukas Homeier, Tracy Li, and Monika H. Schleier-Smith, *Photon-mediated spin-exchange dynamics of spin-1 atoms*, Phys. Rev. Lett. **122**, 010405 (2019).

[37] Dan M. Stamper-Kurn and Masahito Ueda, *Spinor Bose gases: Symmetries, magnetism, and quantum dynamics*, Rev. Mod. Phys. **85**, 1191 (2013).

[38] Kejie Fang, Victor M. Acosta, Charles Santori, Zhihong Huang, Kohei M. Itoh, Hideyuki Watanabe, Shinichi Shikata, and Raymond G. Beausoleil, *High-sensitivity magnetometry based on quantum beats in diamond nitrogen-vacancy centers*, Phys. Rev. Lett. **110**, 130802 (2013).

[39] H. J. Mamin, M. H. Sherwood, M. Kim, C. T. Rettner, K. Ohno, D. D. Awschalom, and D. Rugar, *Multipulse double-quantum magnetometry with near-surface nitrogen-vacancy centers*, Phys. Rev. Lett. **113**, 030803 (2014).

[40] Erik Bauch, Connor A. Hart, Jennifer M. Schloss, Matthew J. Turner, John F. Barry, Pauli Kehayias, Swati Singh, and Ronald L. Walsworth, *Ultralong dephasing times in solid-state spin ensembles via quantum control*, Phys. Rev. X **8**, 031025 (2018).

[41] Emily Davis, Gregory Bentsen, and Monika Schleier-Smith, *Approaching the Heisenberg limit without single-particle detection*, Phys. Rev. Lett. **116**, 053601 (2016).

[42] O. Hosten, R. Krishnakumar, N. J. Engelsen, and M. A. Kasevich, *Quantum phase magnification*, Science **352**, 1552 (2016).

[43] G. Kucsko, S. Choi, J. Choi, P. C. Maurer, H. Zhou, R. Landig, H. Sumiya, S. Onoda, J. Isoya, F. Jelezko, E. Demler, N. Y. Yao, and M. D. Lukin, *Critical thermalization of a disordered dipolar spin system in diamond*, Phys. Rev. Lett. **121**, 023601 (2018).

[44] S. Vega, T. W. Shattuck, and A. Pines, *Fourier-transform double-quantum NMR in solids*, Phys. Rev. Lett. **37**, 43 (1976).

[45] Thomas Bräuniger and Martin Jansen, *Solid-state NMR spectroscopy of quadrupolar nuclei in inorganic chemistry*, Z. Anorg. Allg. Chem. **639**, 857 (2013).

[46] Narayanan Chandrakumar, Ekkehard. Fluck, and Harald Gunther, *Spin-1 NMR* (Springer, New York, 1996), p. 122.

[47] John L Bohn, Ana Maria Rey, and Jun Ye, *Cold molecules: Progress in quantum engineering of chemistry and quantum matter*, Science **357**, 1002 (2017).

[48] S. Lepoutre, J. Schachenmayer, L. Gabardos, B. Zhu, B. Naylor, E. Maréchal, O. Gorceix, A. M. Rey, L. Vernac, and B. Laburthe-Tolra, *Out-of-equilibrium quantum magnetism and thermalization in a spin-3 many-body dipolar lattice system*, Nat. Commun. **10**, 1 (2019).

[49] A. Patscheider, B. Zhu, L. Chomaz, D. Petter, S. Baier, A.-M. Rey, F. Ferlaino, and M. J. Mark, *Controlling dipolar exchange interactions in a dense three-dimensional array of large-spin fermions*, Phys. Rev. Res. **2**, 023050 (2020).

[50] A. V. Gorshkov, M. Hermele, V. Gurarie, C. Xu, P. S. Julienne, J. Ye, P. Zoller, E. Demler, M. D. Lukin, and A. M. Rey, *Two-orbital* SU(N) *magnetism with ultracold alkaline-earth atoms*, Nat. Phys. **6**, 289 (2010).

[51] X. Zhang, M. Bishof, S. L. Bromley, C. V. Kraus, M. S. Safronova, P. Zoller, A. M. Rey, and J. Ye, *Spectroscopic observation of* SU(N)*-symmetric interactions in* Sr *orbital magnetism*, Science **345**, 1467 (2014).

[52] Lucas Gabardos, Bihui Zhu, Steven Lepoutre, Ana Maria Rey, Bruno Laburthe-Tolra, and Laurent Vernac, *Relaxation of the collective magnetization of a dense 3D array of interacting dipolar* $S = 3$ *atoms*, Phys. Rev. Lett. **125**, 143401 (2020).

[53] Emily J. Davis, Avikar Periwal, Eric S. Cooper, Gregory Bentsen, Simon J. Evered, Katherine Van Kirk, and Monika H. Schleier-Smith, *Protecting spin coherence in a tunable Heisenberg model*, Phys. Rev. Lett. **125**, 060402 (2020).

[54] Michael F. O'Keeffe, Lior Horesh, John F. Barry, Danielle A. Braje, and Isaac L. Chuang, *Hamiltonian engineering with constrained optimization for quantum sensing and control*, New J. Phys. **21**, 023015 (2019).

[55] Nikolay V. Vitanov, *Dynamical rephasing of ensembles of qudits*, Phys. Rev. A **92**, 022314 (2015).

[56] Xinxing Yuan, Yue Li, Mengxiang Zhang, Chang Liu, Mingdong Zhu, Xi Qin, Nikolay V. Vitanov, Yiheng Lin, and Jiangfeng Du, *Preserving multi-level quantum coherence by dynamical decoupling*, Phys. Rev. A **106**, 022412 (2022).

[57] Ilia V. Zalivako, Alexander S. Borisenko, Ilya A. Semerikov, Andrey Korolkov, Pavel L. Sidorov, Kristina Galstyan, Nikita V. Semenin, Vasiliy Smirnov, Mikhail A. Aksenov, Aleksey K. Fedorov, Ksenia Yu. Khabarova, and Nikolay N. Kolachevsky, *Continuous dynamical decoupling of optical* $^{171}Yb^{+}$ *qudits with radiofrequency fields*, Front. Quantum. Sci. Technol. **2**, 1228208 (2023).

[58] M. A. Aksenov, I. V. Zalivako, I. A. Semerikov, A. S. Borisenko, N. V. Semenin, P. L. Sidorov, A. K. Fedorov, K. Yu. Khabarova, and N. N. Kolachevsky, *Realizing quantum gates with optically-addressable* $^{171}Yb^{+}$ *ion qudits*, Phys. Rev. A **107**, 052612 (2023).

[59] Cameron J. D. Kemp, Nigel R. Cooper, and F. Nur Ünal, *Nested spheres description of the N-level Chern number and the generalized Bloch hypersphere*, Phys. Rev. Res. **4**, 023120 (2022).

[60] Ryan Barnett, Ari Turner, and Eugene Demler, *Classifying novel phases of spinor atoms*, Phys. Rev. Lett. **97**, 180412 (2006).

[61] H. Makela and K. A. Suominen, *Inert states of spin-S systems*, Phys. Rev. Lett. **99**, 190408 (2007).

[62] E. Serrano-Ensástiga and D. Braun, *Majorana representation for mixed states*, Phys. Rev. A **101**, 022332 (2020).

[63] Pedro Ribeiro, Julien Vidal, and Rémy Mosseri, *Thermodynamical limit of the Lipkin-Meshkov-Glick model*, Phys. Rev. Lett. **99**, 050402 (2007).

[64] O. Giraud, D. Braun, D. Baguette, T. Bastin, and J. Martin, *Tensor representation of spin states*, Phys. Rev. Lett. **114**, 080401 (2015).

[65] C. L. Degen, F. Reinhard, and P. Cappellaro, *Quantum sensing*, Rev. Mod. Phys. **89**, 035002 (2017).

[66] Soonwon Choi, Joonhee Choi, Renate Landig, Georg Kucsko, Hengyun Zhou, Junichi Isoya, Fedor Jelezko, Shinobu Onoda, Hitoshi Sumiya, Vedika Khemani, Curt von Keyserlingk, Norman Y. Yao, Eugene Demler, and Mikhail D. Lukin, *Observation of discrete time-crystalline order in a disordered dipolar many-body system*, Nature (London) **543**, 221 (2017).

[67] A. J. Macfarlane, *Description of the symmetry group* SU *3/Z 3 of the octet model*, Commun. Math. Phys. **11**, 91 (1968).

[68] Shengshi Pang and Andrew N. Jordan, *Optimal adaptive control for quantum metrology with time-dependent Hamiltonians*, Nat. Commun. **8**, 1 (2017).

[69] P. Mansfield, *Symmetrized pulse sequences in high resolution NMR in solids*, J. Phys. C **4**, 1444 (1971).

[70] Leigh S. Martin, Hengyun Zhou, Nathaniel T. Leitao, Nishad Maskara, Oksana Makarova, Haoyang Gao, Qian-Ze Zhu, Mincheol Park, Matthew Tyler, Hongkun Park, Soonwon Choi, and Mikhail D. Lukin, *Controlling local thermalization dynamics in a Floquet-engineered dipolar ensemble*, Phys. Rev. Lett. **130**, 210403 (2023).

[71] Pai Peng, Bingtian Ye, Norman Y. Yao, and Paola Cappellaro, *Exploiting disorder to probe spin and energy hydrodynamics*, Nat. Phys. **19**, 1027 (2023).

[72] N. Leitao *et al.* (to be published).
[73] Wilhelm Magnus, *On the exponential solution of differential equations for a linear operator*, Commun. Pure Appl. Math. **7**, 649 (1954).
[74] Hengyun Zhou, Leigh S. Martin, Matthew Tyler, Oksana Makarova, Nathaniel Leitao, Hongkun Park, and Mikhail D. Lukin, *Robust higher-order Hamiltonian engineering for quantum sensing with strongly interacting systems*, Phys. Rev. Lett. **131**, 220803 (2023).
[75] Hengyun Zhou, Joonhee Choi, Soonwon Choi, Renate Landig, Alexander M. Douglas, Junichi Isoya, Fedor Jelezko, Shinobu Onoda, Hitoshi Sumiya, Paola Cappellaro, Helena S. Knowles, Hongkun Park, and Mikhail D. Lukin, *Quantum metrology with strongly interacting spin systems*, Phys. Rev. X **10**, 031003 (2020).
[76] Hannes Bernien, Sylvain Schwartz, Alexander Keesling, Harry Levine, Ahmed Omran, Hannes Pichler, Soonwon Choi, Alexander S. Zibrov, Manuel Endres, Markus Greiner, Vladan Vuletic, Mikhail D. Lukin, Vladan Vuletić, and Mikhail D. Lukin, *Probing many-body dynamics on a 51-atom quantum simulator*, Nature (London) **551**, 579 (2017).
[77] D. Bluvstein, A. Omran, H. Levine, A. Keesling, G. Semeghini, S. Ebadi, T. T. Wang, A. A. Michailidis, N. Maskara, W. W. Ho, S. Choi, M. Serbyn, M. Greiner, V. Vuletić, and M. D. Lukin, *Controlling quantum many-body dynamics in driven Rydberg atom arrays*, Science **371**, 1355 (2021).
[78] Wil Kao, Kuan-Yu Li, Kuan-Yu Lin, Sarang Gopalakrishnan, and Benjamin L. Lev, *Topological pumping of a 1D dipolar gas into strongly correlated prethermal states*, Science **371**, 296 (2021).
[79] C. J. Turner, A. A. Michailidis, D. A. Abanin, M. Serbyn, and Z. Papić, *Weak ergodicity breaking from quantum many-body scars*, Nat. Phys. **14**, 745 (2018).
[80] Wen Wei Ho, Soonwon Choi, Hannes Pichler, and Mikhail D. Lukin, *Periodic orbits, entanglement, and quantum many-body scars in constrained models: Matrix product state approach*, Phys. Rev. Lett. **122**, 040603 (2019).
[81] Cheng Ju Lin and Olexei I. Motrunich, *Exact quantum many-body scar states in the Rydberg-blockaded atom chain*, Phys. Rev. Lett. **122**, 173401 (2019).
[82] Vedika Khemani, Chris R. Laumann, and Anushya Chandran, *Signatures of integrability in the dynamics of Rydberg-blockaded chains*, Phys. Rev. B **99**, 161101(R) (2019).
[83] Soonwon Choi, Christopher J. Turner, Hannes Pichler, Wen Wei Ho, Alexios A. Michailidis, Zlatko Papić, Maksym Serbyn, Mikhail D. Lukin, and Dmitry A. Abanin, *Emergent* SU(2) *dynamics and perfect quantum many-body scars*, Phys. Rev. Lett. **122**, 220603 (2019).
[84] N. Maskara, A. A. Michailidis, W. W. Ho, D. Bluvstein, S. Choi, M. D. Lukin, and M. Serbyn, *Discrete time-crystalline order enabled by quantum many-body scars: Entanglement steering via periodic driving*, Phys. Rev. Lett. **127**, 090602 (2021).
[85] B. A. Myers, A. Ariyaratne, and A. C. Bleszynski Jayich, *Double-quantum spin-relaxation limits to coherence of near-surface nitrogen-vacancy centers*, Phys. Rev. Lett. **118**, 197201 (2017).
[86] Connor A. Hart, Jennifer M. Schloss, Matthew J. Turner, Patrick J. Scheidegger, Erik Bauch, and Ronald L. Walsworth, *NV-diamond magnetic microscopy using a double quantum 4-Ramsey protocol*, Phys. Rev. Appl. **15**, 044020 (2021).
[87] Priyadharshini Balasubramanian, Christian Osterkamp, Yu Chen, Xiuliang Chen, Tokuyuki Teraji, E. Wu, Boris Naydenov, and Fedor Jelezko, *DC magnetometry with engineered nitrogen-vacancy spin ensembles in diamond*, Nano Lett. **19**, 6681 (2019).
[88] G. Goldstein, P. Cappellaro, J. R. Maze, J. S. Hodges, L. Jiang, A. S. Sørensen, and M. D. Lukin, *Environment-assisted precision measurement*, Phys. Rev. Lett. **106**, 140502 (2011).
[89] Jing Liu, Haidong Yuan, Xiao-Ming Lu, and Xiaoguang Wang, *Quantum Fisher information matrix and multiparameter estimation*, J. Phys. A **53**, 023001 (2019).
[90] Esteban A. Martinez, Christine A. Muschik, Philipp Schindler, Daniel Nigg, Alexander Erhard, Markus Heyl, Philipp Hauke, Marcello Dalmonte, Thomas Monz, Peter Zoller, and Rainer Blatt, *Real-time dynamics of lattice gauge theories with a few-qubit quantum computer*, Nature (London) **534**, 516 (2016).
[91] Bing Yang, Hui Sun, Robert Ott, Han Yi Wang, Torsten V. Zache, Jad C. Halimeh, Zhen Sheng Yuan, Philipp Hauke, and Jian Wei Pan, *Observation of gauge invariance in a 71-site Bose–Hubbard quantum simulator*, Nature (London) **587**, 392 (2020).
[92] Monika Aidelsburger *et al.*, *Cold atoms meet lattice gauge theory*, Phil. Trans. R. Soc. A **380**, 20210064 (2021).
[93] Zhao Yu Zhou, Guo Xian Su, Jad C. Halimeh, Robert Ott, Hui Sun, Philipp Hauke, Bing Yang, Zhen Sheng Yuan, Jürgen Berges, and Jian Wei Pan, *Thermalization dynamics of a gauge theory on a quantum simulator*, Science **377**, 311 (2022).
[94] Daniel González-Cuadra, Torsten V. Zache, Jose Carrasco, Barbara Kraus, and Peter Zoller, *Hardware efficient quantum simulation of non-Abelian gauge theories with qudits on Rydberg platforms*, Phys. Rev. Lett. **129**, 160501 (2022).
[95] Maarten Van Damme, Torsten V. Zache, Debasish Banerjee, Philipp Hauke, and Jad C. Halimeh, *Dynamical quantum phase transitions in spin-S* $U(1)$ *quantum link models*, Phys. Rev. B **106**, 245110 (2022).
[96] Jad C. Halimeh, Lukas Homeier, Annabelle Bohrdt, and Fabian Grusdt, *Spin exchange-enabled quantum simulator for large-scale non-Abelian gauge theories*, arXiv:2305.06373.
[97] Jesse Osborne, Bing Yang, Ian P. McCulloch, Philipp Hauke, and Jad C. Halimeh, *Spin-S U(1) quantum link models with dynamical matter on a quantum simulator*, arXiv:2305.06368.
[98] N. Y. Yao, C. R. Laumann, A. V. Gorshkov, S. D. Bennett, E. Demler, P. Zoller, and M. D. Lukin, *Topological flat bands from dipolar spin systems*, Phys. Rev. Lett. **109**, 266804 (2012).
[99] Martin Garttner, Justin G. Bohnet, Arghavan Safavi-Naini, Michael L. Wall, John J. Bollinger, and Ana Maria Rey, *Measuring out-of-time-order correlations and multiple*

quantum spectra in a trapped-ion quantum magnet, Nat. Phys. **13**, 781 (2017).

[100] T. C. Ralph, K. J. Resch, and A. Gilchrist, *Efficient Toffoli gates using qudits*, Phys. Rev. A **75**, 022313 (2007).

[101] A. S. Nikolaeva, E. O. Kiktenko, and A. K. Fedorov, *Efficient realization of quantum algorithms with qudits*, arXiv:2111.04384.

[102] Jonathan M. Baker, Casey Duckering, and Frederic T. Chong, *Efficient quantum circuit decompositions via intermediate qudits*, in *Proceedings of the IEEE 50th International Symposium on Multiple-Valued Logic (ISMVL), Miyazaki, Japan* (2020), pp. 303–308, 10.1109/ISMVL49045.2020.9345604.

[103] Pranav Gokhale, Jonathan M. Baker, Casey Duckering, Frederic T. Chong, Natalie C. Brown, and Kenneth R. Brown, *Extending the frontier of quantum computers with qutrits*, IEEE Micro **40**, 64 (2020).

[104] Sam R. Cohen and Jeff D. Thompson, *Quantum computing with circular Rydberg atoms*, PRX Quantum **2**, 030322 (2021).